

BCG alignment with the Locations of Cluster Members and the Large Scale Structure out to 10 R_{200}

Rory Smith^{1*}, Ho Seong Hwang,^{2,3,4} Katarina Kraljic^{5,6} Paula Calderón-Castillo,¹ Thomas M. Jackson,^{7,8}

Anna Pasquali,⁸ Jihye Shin,⁴ Jongwan Ko,^{4,9} Jaewon Yoo,¹⁰ Hyowon Kim,⁹ and Jae-woo Kim,⁴

¹*Departamento de Física, Universidad Técnica Federico Santa María, Avenida Vicuña Mackenna 3939, San Joaquín, Santiago de Chile*

²*Astronomy Program, Department of Physics and Astronomy, Seoul National University, 1 Gwanak-ro, Gwanak-gu, Seoul 08826, Republic of Korea*

³*SNU Astronomy Research Center, Seoul National University, 1 Gwanak-ro, Gwanak-gu, Seoul 08826, Republic of Korea*

⁴*Korea Astronomy and Space Science Institute (KASI), 776 Daedeokdae-ro, Yuseong-gu, Daejeon 34055, Korea*

⁵*Université de Strasbourg, CNRS UMR 7550, Observatoire astronomique de Strasbourg, 11 rue de l'Université, 67000 Strasbourg, France*

⁶*Aix Marseille Université, CNRS, CNES, UMR 7326, Laboratoire d'Astrophysique de Marseille, Marseille, France*

⁷*Tuparev AstroTech, 3 Sofiyski geroy Str., entr. 2 app. 28, Sofia 1612, Bulgaria*

⁸*Astronomisches Rechen-Institut, Zentrum für Astronomie der Universität Heidelberg, Mönchhofstraße 12-14, 69120 Heidelberg, Germany*

⁹*University of Science and Technology (UST), Daejeon 34113, Korea*

¹⁰*Quantum Universe Center, Korea Institute for Advanced Study, 85 Hoegi-ro, Dongdaemun-gu, Seoul 02455, Korea*

Accepted to MNRAS August 2023

ABSTRACT

Using a sample of > 200 clusters, each with typically 100 – 200 spectroscopically confirmed cluster members, we search for a signal of alignment between the Position Angle (PA) of the Brightest Cluster Galaxy (BCG) and the distribution of cluster members on the sky about the cluster centre out to projected distances of 3 R_{200} . The deep spectroscopy, combined with corrections for spectroscopic incompleteness, makes our sample ideal to determine alignment signal strengths. We also use an SDSS based skeleton of the filamentary Large Scale Structure (LSS), and measure BCG alignment with the location of the LSS skeleton segments on the sky out to projected distances of 10 R_{200} . The alignment signal is measured using three separate statistical measures; Rao's spacing test (U), Kuiper's V parameter (V), and the Binomial probability test (P). The significance of the BCG alignment signal with both cluster members and LSS segments is extremely high (1 in a million chance or less to be drawn randomly from a uniform distribution). We investigate a wide set of parameters that may influence the strength of the alignment signal. Clusters with more elliptical-shaped BCGs show stronger alignment with both their cluster members and LSS segments. Also, selecting clusters with closely connected filaments, or using a luminosity-weighted LSS skeleton, increases the alignment signal significantly. Alignment strength decreases with increasing projected distance. Combined, these results provide strong evidence for the growth of clusters and their BCGs by preferential feeding along the direction of the filaments in which they are embedded.

Key words: galaxies: clusters: general – galaxies: general – cosmology: large-scale structure of Universe

1 INTRODUCTION

It has long been known that, in the nearby Universe, the shape of the spatial distribution of the cluster members tends to be preferentially aligned with the position angle of the major axis (PA) of the Brightest Cluster Galaxy (BCG; Sastry 1968), referred to as 'BCG-cluster alignment'. Since then, the advent of wide-field surveys such as the Sloan Digital Sky Survey (SDSS; York et al. 2000) has enabled the study of BCG-cluster alignment using huge statistical samples of clusters, and allowed us to study which parameters dictate the strength of the alignment. Niederste-Ostholt et al. (2010) used SDSS DR6 data to study several thousands of clusters, and noted a tendency for richer clusters to show stronger alignment. Huang et al. (2016) used SDSS DR7 (Abazajian et al. 2009) data for a similarly large

number of clusters, that were selected using the redMaPPer cluster finding algorithm (Rykoff et al. 2014). They tested a large set of parameters such as central and satellite luminosity, central size, colour, and found that the shape of the central galaxy was an important parameter. However, these studies could not spectroscopically confirm that all of their satellite samples are truly satellites, due to the shallow depth of the SDSS spectroscopy. Using the deeper spectroscopy of the GAMA survey, Georgiou et al. (2019) found a sensitive dependence of alignment strength on galaxy colour. Similarly, Rodriguez et al. (2022) used SDSS DR16 data and found that central colour of the group was a key parameter, although central shape and group mass did not play a clear role in their results. While many studies primarily focused on the locations of satellites based on optical observations, it has since been shown that the BCG-cluster alignment is also revealed when observing the cluster shape with X-rays, the

* E-mail: rorysmith274@gmail.com

Sunyaev–Zeldovich Effect, and using gravitational lensing as well (Donahue et al. 2016; Yuan & Wen 2022).

There is some debate in the literature over whether the BCG-cluster alignment strength evolves with time. Although limited by the redshift range of their sample (typically less than $z = 0.4$), Niederste-Ostholt et al. (2010) and Hao et al. (2011) found a significant reduction in alignment strength towards higher redshifts. However, over a similar redshift range, Huang et al. (2016) failed to find any significant evolution. The West et al. (2017) sample spans a much larger redshift range, from $z = 0.19$ to 1.8, and they found evidence for alignment in their highest redshift clusters, when the Universe was only one third of its current age. Recently, the evolution of BCG-cluster alignment was studied using cosmological simulations, and it was found that alignment has been in place since $z \sim 4$, and there has been little evolution of its strength since $z = 2$ (Ragone-Figueroa et al. 2020).

The main theories for the origin of BCG-cluster alignment are: primordial alignment with the surrounding matter distribution at the time of galaxy formation, gravitational torques that gradually align galaxies with the local tidal field, and/or anisotropic infall of matter into clusters along preferred directions (Catelan & Theuns 1996; West 1994; Libeskind et al. 2013). In a realistic cosmological setting, these different origin scenarios cannot occur fully independently of each other (Faltenbacher et al. 2008). Thus, the observed phenomena are likely an inseparable combination of all three theories. For example, West (1994) noted that the mergers which build up BCGs do not occur haphazardly, but rather along preferred axes related to large-scale anisotropies in the primordial density field. The significance of mergers occurring along preferred directions is further emphasised in Wittman et al. (2019). Using a sample of clusters undergoing major mergers, they found that the cluster shape is aligned with the merger axis, defined by a line joining the two brightest galaxies in the cluster. Using cosmological simulations of clusters, Ragone-Figueroa et al. (2020) found that major mergers can either strengthen, weaken or have no effect on the BCG alignment with the cluster, depending on the direction of the accretion. However, interestingly BCGs that become misaligned by a merger tended to reorientate themselves back into alignment on several gigayear timescales, in part due to tidal torques.

The importance of mergers in driving the BCG-cluster alignment is further emphasised by the fact that the alignment strength decreases significantly when the PA of the second brightest cluster galaxy is used instead. Indeed, the alignment disappears altogether if the third brightest cluster galaxy or fainter galaxies are used (Torlina et al. 2007; Niederste-Ostholt et al. 2010; Sifón et al. 2015; West et al. 2017, although see Huang et al. 2018). This underlines the unique conditions the BCGs experience in their clusters. As they are generally the central galaxy of the cluster, they suffer many mergers as the cluster grows by accretion.

This subsequent feeding of clusters along preferential axes means the cluster shape must have some dependence on the surrounding large-scale environment. Environmental density appears to play a role in the strength of the BCG-cluster alignment (Wang et al. 2018), and simulations show that the halo shape is also a function of environmental density (Ragone-Figueroa & Plionis 2007). Using the cross-correlation of Lick galaxy counts, Argyres et al. (1986) and Lambas et al. (1988) note a preference for alignment with the BCG PA out to distances ~ 15 Mpc. Similarly, Paz et al. (2011) find a signal of correlation between cluster shape and the surrounding galaxies out to 30 Mpc. The filamentary structure of the large-scale environment provides a natural manner by which clusters may be fed preferentially down the filament axes. In simulations, Codis et al.

(2018) find that in particular massive galaxies tend to have spins that are orthogonal to, and shapes that are extended along their filaments, and the strength of this coherence increases with time. This form of spin alignment is driven by spin reorientation due to mergers (Welker et al. 2018). The infall of galaxies down filaments is thought to generate an overall rotation in some observed clusters (Song et al. 2018). Simulations also show that clusters connected to larger numbers of filaments are more elliptical, later formed, and more unrelaxed (Daragh Ford et al. 2019; Gouin et al. 2021). Furthermore, galaxies with more connections have been shown (in observations and simulations) to be more elliptical, redder and with lower specific star formation rates (Kraljic et al. 2020). However, in the complex tidal field of super-clusters, some clusters are observed to have become disconnected from the Large Scale Structure (LSS), leaving behind orphaned filaments (Einasto et al. 2020, 2021).

In this study, we seek to directly link the position angle of cluster BCGs to their cluster shape as measured using spectroscopically classified cluster members. One advantage of our study is that our cluster sample has been the subject of several extensive spectroscopic surveys (e.g. Rines et al. 2013, 2018, 2016; Hwang et al. 2014) with MMT/HectoSPEC. This provides us with a large sample (~ 200) of clusters, each with spectroscopically confirmed cluster members out to several R_{200} from the cluster centre. In this way, we can test for a signal of alignment between BCG PA and cluster members with a large sample of clusters with a reliable and deep sample of their members. Additionally, the availability of SDSS imaging allows us to include corrections for spectroscopic incompleteness to try to correct our alignment signal measures for uneven completeness about the cluster centre.

For a selection of these clusters, we complement this data with a map of the Large Scale Structure, built using redshifts from the main galaxy sample of the SDSS survey using the code DisPerSE (Discrete Persistent Structure Extractor code; Sousbie 2011). This allows us to trace out the filamentary skeleton of the LSS out to $10 R_{200}$, in order to test for alignment between the BCG PA at radii far beyond the cluster vicinity, as well as consider how parameters such as the number of filament connections and distance to closest filament impact on the alignment strength.

This work is organized as follows. In Section 2, we describe our sample selection and in Section 3 we explain our method. In Section 4 we present our results. Finally, in section 5, we discuss the results and summarise them.

Throughout the paper, we adopt a standard Λ CDM cosmology with $\Omega_M = 0.3$, $\Omega_\Lambda = 0.7$ and $h = 0.7$. Magnitudes are given in the AB system. All the results here are based on the 16th Data Release of the Sloan Digital Sky Surveys (DR16, Ahumada et al. 2020).

2 SAMPLE

2.1 The Cluster Sample

Our total sample consists of 211 X-ray selected clusters where we have dedicated redshift surveys other than the SDSS within the SDSS footprint. These include 58 from the HectoSPEC Cluster Survey (HeCS; Rines et al. 2013), 121 from HeCS-red (Rines et al. 2018), 123 from HeCS-SZ (Rines et al. 2016), 9 from the weak-lensing cluster survey (Hwang et al. 2014), and 2 clusters from OmegaWINGS (Moretti et al. 2017). We have also included 72 Cluster Infall Region Survey clusters (CIRS; Rines & Diaferio 2006) that have the SDSS data along with the redshifts from the NASA/IPAC Extragalactic

Database (NED¹). As there are several clusters in common between the various surveys, the final number of clusters is 211. These clusters were mainly selected to take advantage of simultaneous coverage by SDSS for optical wavelengths and ROSAT (Voges et al. 1999) for X-ray coverage. The clusters range in mass from $M_{200} = 1 \times 10^{13} M_{\odot}/h$ to $1 \times 10^{15} M_{\odot}/h$ (although 70% are between $1 - 5 \times 10^{14} M_{\odot}/h$). These masses were determined dynamically using the caustic technique, while the cluster centres are determined based on their X-ray centres (see Rines et al. 2013 for details). They range in redshift from $z = 0.003 - 0.289$ with a mean of $z = 0.117$. A full list of the clusters and their properties can be found in columns (i)-(vii) of Table B1, and the redshift survey from which they are drawn is given in column (x).

All the redshift estimates are collected from the literature listed above, and combined with those in the SDSS DR16. Typically, MMT/HectoSPEC spectroscopy from those papers was conducted on $\sim 400 - 600$ candidate cluster members per cluster. These cluster member candidates were mainly selected using the red sequence technique (Gladders & Yee 2000), based on SDSS panchromatic photometry, meaning the selected galaxies are generally biased towards early-type galaxies. We also supplement these redshifts with additional redshift measurements from NED which are typically less biased toward early-type galaxies. Cluster members were then identified using the caustic technique (Diaferio 1999). The number of cluster members found varies widely between individual clusters (from ~ 20 to greater than 1000 and depends on the cluster mass), but generally our clusters have large numbers of identified members. For example, 70% of the clusters have > 100 spectroscopically confirmed cluster members. The wide field-of-view of HectoSPEC allows cluster members to be typically identified out to several R_{200} from the clusters. 193 clusters (91%) have confirmed members beyond $2 R_{200}$ and 149 clusters (70%) have confirmed members beyond $3 R_{200}$. Targets were prioritised according to their apparent magnitude and their distance from the cluster centre. This means galaxy completeness falls rapidly for galaxies fainter than $r = 19.5$ for HeCS clusters (17.77 for CIRS clusters), hence we cut our sample for galaxies fainter than these limiting magnitudes. The limiting magnitude for each cluster is given in column (viii) of Table B1. We further correct for incompleteness by comparing to SDSS galaxy catalogues in the same field. We can then calculate the spectroscopic completeness for the galaxies in the cluster field, which is measured in R_{200} -sized square apertures on the sky around the cluster's location. With this, we can introduce corrections to our counts of galaxies on the sky about the cluster centre. This reduces the impact of uneven completeness as a function of distance from the cluster centre and for varying position angle on the sky on our measured alignment signals. We also test if the strength of the alignment depends on a measure of the overall cluster completeness in Section 4.3.

For BCGs and all cluster members, we also consider their position angle on the sky about the cluster centre, and their galaxy shape (*bla* axial ratio). The galaxy shape is from the best-fit parameters of the SDSS images with the de Vaucouleurs fit, which are provided by the SDSS Skyserver DR16 (Stoughton et al. 2002). We adopt these values in the r-band as the use of a filter which collects red optical light means we are less impacted by bright star-forming regions, and the data is relatively deep. We compare to measurements in the i-band and generally find very good agreement (e.g., 90% of PAs

agree within 2 degrees). In general, the criteria for choosing the BCG within the cluster is to select the brightest spectroscopically confirmed cluster member within a projected radius of $0.5 R_{200}$ of the cluster centre. We visually check each case as occasionally the brightest object is a star that has been misclassified as a galaxy, or the BCG was too bright to be included in the SDSS redshift survey, or the galaxy shape and position angle is poorly defined due to close galaxy pairs or pixel-bleeding. The BCG parameters for each cluster are given in columns (xi)-(xv) of Table B1.

2.2 The Large Scale Structure Surrounding Clusters

In order to search for alignment between the BCG PA with the Large Scale Structure (LSS) surrounding the cluster, we first build an LSS map based on galaxy redshifts from the SDSS survey. Initially, we choose a sample of galaxies brighter than the magnitude limit of the SDSS main galaxy sample for uniformity (i.e. $m_r < 17.77$; Strauss et al. 2002). We first run the Friends-of-Friends algorithm with a variable linking length following Tempel et al. (2014). This is to take into account the effect that the galaxy number density changes with redshift in the magnitude-limited sample. We therefore compute the mean galaxy separation at each redshift (d_{mean}), and adopt the linking lengths of $0.2 d_{\text{mean}}$ perpendicular to the line of sight and $1 d_{\text{mean}}$ along the line of sight. These linking lengths correspond to 1 and $5 h^{-1}$ Mpc, respectively, at the median redshift of the sample (i.e. $z \sim 0.1$). We can then correct the 3D location of these galaxies for the finger-of-god effect by assuming that the group shape and dispersion is symmetrical perpendicularly and along our line of sight (Kraljic et al. 2018, see also Tegmark et al. 2004; Hwang et al. 2016).

Now, with the 3D locations of the galaxies, we extract the skeleton of the filamentary LSS structure surrounding our clusters using the publicly available code DisPerSE (Sousbie 2011; Sousbie et al. 2011)², run with a 5σ persistence threshold on the distribution of galaxies. This choice allows us to easily identify the larger and more dense filaments typically found connected to clusters. A lower value of the persistence would recover less substantial filaments, and potentially inject more noise into the alignment measurement.

As more massive galaxies tend to be found closer to filaments, we weight the Delaunay tessellation (see Sousbie 2011, for detailed description of the DisPerSE code) by the galaxy luminosities. In Section 4.2, we will see that weighting by galaxy luminosity can significantly influence the strength of the alignment signal.

Although we have information on the cluster members for the full sample of 211 clusters, our LSS skeleton is only constructed for objects within the main SDSS area and some of the HeCS clusters fall outside this footprint. Those clusters that fall inside this footprint are labelled 'LSS' in column (xvi) of Table B1. Therefore, we cannot study the alignment with the LSS for all of the clusters. Also, we require that the LSS skeleton connects directly with the cluster in three-dimensions – our criteria is that at least one segment must cross a sphere of $3 R_{200}$ centred on each cluster ($R_{200,\text{connect}} = 3 R_{200}$), and we exclude any unconnected filaments from our analysis. In Section 4.2, we test the sensitivity of our results to this fairly arbitrary choice of value for $R_{200,\text{connect}}$. Finally, when studying the BCG PA alignment with the LSS, we exclude clusters that have another cluster within $5 R_{200}$ (Near Pair, $NP > 5 R_{200}$). This reduces the presence of numerous galaxies or LSS segments associated with the other cluster as a noise source in our measured alignment signal. Additionally, we test how this choice of distance affects our results in Section 4.2.

¹ The NASA/IPAC Extragalactic Database (NED) is operated by the Jet Propulsion Laboratory, California Institute of Technology, under contract with the National Aeronautics and Space Administration.

² <http://www2.iap.fr/users/sousbie/web/html/indexd41d.html>

2.3 The ‘Cluster Members-only’ sample versus the ‘Cluster Members + LSS’ sample

As a result of the various restrictions described in Section 2.2, our full sample of 211 clusters with spectroscopically confirmed members is reduced to 91 clusters, if we require the information on their surrounding LSS for our analysis. Thus, we refer to this sample as the ‘Cluster Members + LSS’ sample, and we always use this sample when studying BCG alignment with the LSS, and the dependency of the alignment on LSS parameters (e.g., number of filament connections, etc). We consider the results for BCG alignment measured using this sample in Section 4.1 and 4.2.

However, we can use the full sample of 211 clusters if we restrict ourselves to consider alignment between the BCG PA and their cluster members only, neglecting the alignment with the LSS. We refer to this sample as the ‘Cluster Members-only’ sample, and consider this sample’s alignment results separately in Section 4.3. By using the ‘Cluster Members-only’ sample, we can greatly increase our number statistics. For example, the fiducial model of the ‘Cluster Members-only’ sample consists of 13,741 galaxies compared to 5,917 member galaxies in the ‘Cluster Members + LSS’ sample.

3 METHOD

We can now begin to search for a signature of alignment between the PA and the location of cluster members/LSS segments on the sky. Our method for doing this is as follows.

We first measure the typical strength of the alignment for the cluster sample as a whole. This is accomplished by stacking multiple clusters together, after rotating each cluster individually so as their BCG PAs are aligned vertically on the stacked image. By stacking, we can average out some of the noise that may exist in individual clusters, and we can also greatly increase the number of cluster members and/or LSS segments that are used to measure the strength of the alignment.

Then, we can simply compute each satellite galaxy’s PA on the sky, measured from the cluster centre. We then calculate the difference between this PA and that of the BCG PA.

For the LSS, the approach is similar. DisPerSE filaments consist of a series of linear segments with two endpoints. To measure the BCG alignment with the segments, we measure the position angle of each segment on the sky, measured with respect to the cluster centre, and compare with the BCG PA. We note that an alternative means to measure the alignment with the segments would be to measure the position angle of one end of a segment from the other end, and compare that with the BCG PA. However, this alternative approach is likely more sensitive to segment-to-segment deviations³. Therefore, in this study we focus on the use of segment positions on the sky about the cluster centre instead.

We wish to know if the alignment signal extends to distances far beyond the influence of the cluster. Therefore, we divide our sample into radial bins by their projected radius from the cluster centre. For the LSS segments the radial bins are $0 - 3 R_{200}$, $3 - 6 R_{200}$ and $6 - 10 R_{200}$. For the cluster members, we test radial bins of $0 - 1 R_{200}$, $1 - 2 R_{200}$ and $2 - 3 R_{200}$. We also consider the case where all the radial bins are combined ($0 - 10 R_{200}$ for the LSS segments, and $0 - 3 R_{200}$ for the cluster members) in order to maximise the statistics.

Following West et al. (2017), we consider three separate statistical methods to quantify the strength of the BCG alignment signal; the

Rao-spacing test, Kuiper’s V-statistic and the Binomial test (referred to as the measures U , V and P respectively from herein). One strength of these methods is that there is no requirement for arbitrary binning of the PAs of the galaxies/LSS segments about the cluster center.

3.1 The Rao-Spacing test, U

For a sample of size N with a perfectly uniform distribution, galaxies/LSS segments should have offsets from the BCG PA that are evenly spaced between 0 and 90 degrees:

$$\lambda = \frac{90}{N}, \quad (1)$$

where λ is the expected spacing of a uniform distribution. The Rao-spacing test measures the amount of deviation from the case of even spacing, and can be defined as

$$U = \frac{1}{2} \sum_{i=1}^{N-1} |\theta_i - \lambda|, \quad (2)$$

where θ_i is the angular offset of the i th object from the BCG PA, $T_i = \theta_{i+1} - \theta_i$ for $i \leq N - 1$, and $T_i = (90 - \theta_N) + \theta_1$ for $i = N$.

In practice, the sample’s PA values are sorted by size such that the angle between successive values can be easily measured. Because of the summation of deviations from the uniform case, the U value is larger for a less uniform distribution. However, we note that the U measure may also be enhanced if the distribution of PAs is clumpy, rather than simply preferring a single direction on the sky.

3.2 Kuiper’s V-statistic, V

To measure Kuiper’s V-statistic, the PAs are once again sorted into increasing order and a cumulative distribution of their values is made from 0 to 90 degrees. The maximum value of the cumulative distribution above that of a pure uniform distribution is assigned to the D_+ variable. The minimum value of the cumulative distribution below that of a pure uniform distribution is assigned to the D_- variable. Kuiper’s V-statistic is then simply given by their summation:

$$V = D_+ + D_-. \quad (3)$$

As a result, if the galaxy/LSS segment PAs prefer a particular direction, such as the BCG PA, the value of V will increase.

3.3 The Binomial test, P

For the Binomial test value P , the fraction of objects which have a difference in PA with respect to the BCG PA of less than 45 degrees is measured. For a perfectly uniform sample, $P=0.5$, whereas if the positions of the objects on the sky show a preference for alignment with the BCG PA, $P > 0.5$.

3.4 Significance of alignment measurements

Again, following the procedure outlined in West et al. (2017), we test the significance of the three alignment measures (U , V and P) by calculating their probability for such a value to be drawn by chance from a uniform distribution (P_{uniform}). First, we generate one million samples, of equal size to the observed sample, whose PAs are randomly drawn from a uniform distribution. For each sample, we

³ Testing with this alternative measure recovers qualitatively similar results.

measure its U , V and P value. Then, to calculate P_{uniform} , we measure what fraction of the million samples reaches the observed values. If none of the samples reaches the observed value, the P_{uniform} must be less than one in a million (i.e., highly non-uniform). For the figures presented in this paper (Section 4), we only keep data points where there is a 1 in 44 chance or less that the sample could be drawn by chance from a uniform sample (equivalent to a two-sigma or higher detection of non-uniformity). This establishes a minimum level of non-uniformity within our results, and helps to remove false trends that could be produced by chance, in particular when statistics are limited. In addition, the error bars on data points (see next section for a description) can also help us judge the significance of any observed trends.

3.5 Comparing Subsamples of equal size

Rather than simply stacking all the clusters together, we can also experiment with subsampling the cluster sample. In this way, we can choose which clusters to include in the stack, and test dependencies of the BCG alignment signal strength on various parameters of our choice. For example, comparing high- and low-mass clusters, or producing a low-redshift cluster sample. An individual galaxy may belong to multiple subsamples (e.g., Nearby Universe and Luminosity). Also, depending on how the subsample is divided, an individual galaxy may appear on both sides of the divide (e.g., a bright galaxy in the Luminosity subsample could appear in the ‘All’ and ‘Bright’ category). In the same way, clusters may also belong to multiple subsamples, or both sides of the divide of a subsample, depending on how the divide is defined (e.g., a cluster will only fall in either the round or the elliptical category but it will always be found in the Fiducial category.) A full list of the subsamples considered is given in Section 4.2 for the alignment with the LSS and in Section 4.3 for the alignment with the cluster members.

In order to allow a fair comparison of U , V and P values between subsamples, we ensure that we only compare subsamples of equal size. The reduction in the size of a subsample is achieved by randomly selecting from the original subsample (of size N_{orig}) until it reaches a sample size that is the minimum among the compared subsamples (N_{min}). However, the final measurement of U , V and P may depend on which objects were selected for the reduced subsample. For the V and P measurements, we measure the uncertainties introduced by the subsample reduction by conducting 1000 bootstraps of the selection of N_{min} objects from the original N_{orig} objects, and measuring the mean value of V and P with their error given by the standard deviation. However, it is impossible to treat the U values similarly, as bootstrapping results in objects in the reduced sample with repeated (identical) PA values. As U is influenced by the separation between consecutive PA values that have been ordered by size (see Section 3.1), it is strongly enhanced by repeated values. Therefore, in the case of the U measurement, we instead randomly select N_{min} objects from the original N_{orig} objects without any repetition of PA values. This process is repeated 1000 times and U is assigned the mean value with an error given by the standard deviation. The number of objects in each of the subsamples (e.g., galaxies, LSS segments and clusters) is provided in Appendix C (Tables C1 – C4).

4 RESULTS

4.1 Visual representation of BCG Alignment in the ‘Cluster Members + LSS’ sample

We start by considering our sample of clusters with information on their surrounding LSS (see Section 2.2 for details). The total number of clusters is 91.

In the top-left panel of Figure 1, we plot the number density of the stacked cluster members (after each cluster has been rotated such that their BCG PA is always vertical). The x- and y-axis are normalised by R_{200} and we overlay circles with radii of 1, 2 and 3 R_{200} to better highlight the shape of the cluster member distribution which is extended along the BCG PA in both directions, as further highlighted by the contours of equal galaxy number density. In any individual cluster, the distribution of galaxies might be more extended in one direction than in the other. However, when we stack multiple clusters, the resulting cluster member distribution tends to be symmetrical vertically. This is because, when the BCG PA is defined, it could point in either direction with equal probability.

In the top-right panel, we plot the number of cluster members in bins of position angle for all the stacked clusters. For this visual representation, we use a fairly arbitrarily chosen bin width of 30 degrees, where the first bin is positioned symmetrically about the vertical axis in the top-left panel. We note that this binning is only used for this visual demonstration of the alignment. All measures of the BCG alignment signal strength are conducted using the bin-free statistical measures that we previously described in Section 3. Here, we show a separate histogram of the number of cluster members for the three projected radial bins. The elliptical shape of the cluster members distribution about the cluster centre that was visible in the upper-left panel is also clearly visible in these histograms with similar-sized peaks at 0/360 and 180 degrees.

The bottom sub-panel shows that the average completeness is roughly equal in all angular bins, and thus the alignment with the satellite members is not a result of preferentially higher completeness in angle bins near the BCG PA. We present the completeness-corrected histogram as a filled area, and the histograms without completeness correction as a solid line. Note that the curve of the uncorrected histogram can be higher in some angle bins than the corrected histogram as the latter has been re-normalized to match the total sample size of the uncorrected histogram.

In the lower-left panel, we consider the stacked plot of all of the LSS skeletons that are connected to clusters at 3 R_{200} either directly or indirectly. Visibly, it can be seen that there is a tendency for more filaments to emerge from the top and bottom of the clusters (i.e. parallel to the BCG PA) compared to from left to right (perpendicular to the BCG PA). We place a translucent circle of radius 1 R_{200} at the centre to try to make this more visible. While the filaments that emerge from the bottom are quite vertically aligned, those emerging from the top appear slightly tilted with respect to the BCG PA. The histograms in the lower-right panel confirm that this is the case, with a well-aligned peak at 0/360 degrees in the first and second radial bin, but the other peak has a slight offset from 180 degrees. We hypothesise that this may be the result of the low number statistics of clusters considered in this stack. Nevertheless, it is clear that, far from being uniformly distributed, there is a tendency for the filaments to be more aligned with the BCG PA over the full 0 – 10 R_{200} range.

The measured U , V , and P values for the stack of all the LSS segments of our ‘Fiducial’ model (91 clusters in the sample) are $U=35.4$, $V=684.6$, and $P=0.58$ for all the radial bins combined (0–10 R_{vir}). All the results are highly significant – a by chance selection of the PA distribution from a uniform distribution is ruled out at a

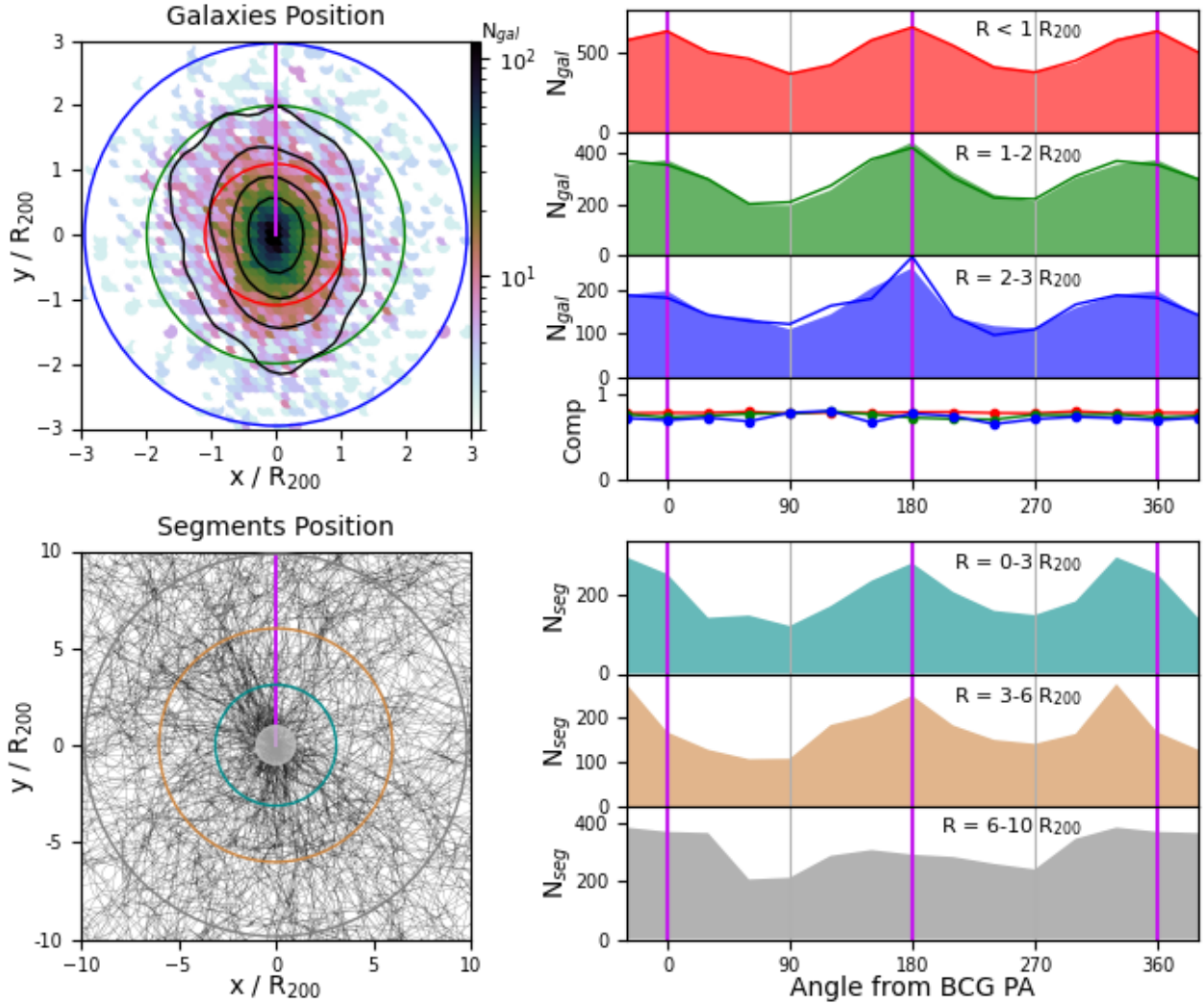


Figure 1. Results of stacking all the ‘Cluster Members + LSS’ sample. Top-left: Stack of the position of the cluster members after rotating each cluster to align their BCG PAs vertically along the purple line. The x- and y-axis are normalised by the R_{200} of each individual cluster. The colour bar indicate the number of galaxies in a pixel of length 120 pc, and black iso-number contours are overlaid, to highlight the extended shape of the cluster members along the BCG PA. The coloured circles show the three bins of projected radius we consider (red, green, blue is $0 - 1$, $1 - 2$, $2 - 3 R_{200}$, respectively). Top-right: Histograms of the angle of cluster members about the cluster centre, measured with respect to the BCG PA. The top three subpanels match the radial bins in the top-left panel. Purple vertical lines highlight where an alignment signal should result in peaks, with grey vertical lines for troughs. The lowest subpanel shows the mean completeness in each angular bin, with a different colour line for each radial bin. The shaded histograms are the renormalised completeness corrected number counts while the solid lines are not completeness corrected. Bottom-left: As in the top-left panel, but stacking the LSS segments that are connected to the cluster. We place a $1 R_{200}$ radius translucent sphere over the cluster to try to highlight where the filaments leave from the cluster. Bottom-right: As in the top-right panel, but histograms of the number of LSS skeleton segments in each angular bin. There is no completeness subpanel as the SDSS completeness is very uniform.

one in a million (or greater than million) level (non-uniform at the level of $>4.8\sigma$). The alignment signal is also highly significant in the individual radial bins as well. All are non-uniform at a one in $>$ one million level, except for the first radial bin of the U measure which is non-uniform at a one in $>$ 100 thousand level (still highly significant, $>3.9\sigma$).

4.2 Results of subsampling the ‘Cluster Members + LSS’ sample

We split the ‘Cluster Members + LSS’ sampling according to five different parameters described below. As noted in Section 3, each subsample is of equal size to enable a fair comparison of the measured

U , V and P parameters, free from the effects of changing subsample size. The subsampling approach is described in Section 3.5. However, this means that comparisons of alignment signal strength should only be done *within a subsample, and for matching radial bins*. The results are shown in Figure 2. Data points whose probability to be uniform is too high (i.e., P_{uniform} is greater than our chosen criteria, described in Section 3.4) are removed from the panels. Error bars arising from the subsampling procedure are calculated as described in Section 3.5.

- **BCG Shape:** The BCG shape is quantified by the axial ratio (b/a) of the BCG from the best-fit parameters of the SDSS DR16 (Ahumada et al. 2020). We split the sample into ‘Elliptical’ BCGs

(with $b/a < 0.75$) and ‘Round’ BCGs ($b/a \geq 0.75$) in the first column of Figure 2 (cluster sample sizes of 48 and 43 respectively). In the ‘Fiducial’ subsample, no shape limit was imposed. For all three measurements (U , V and P) where the radial bins are combined (0-10 R_{200}), the clusters with ‘elliptical’ BCGs have a significantly higher alignment signal. For the V and P measures of the combined radial bins, the clusters with ‘round’ BCGs are those with the lowest signal strength and they are significantly lower. For example, comparing clusters with round versus elliptical BCGs, $V = 180.0 \pm 23.0$ versus $V = 439.7 \pm 0.27.9$, and $P = 0.528 \pm 0.008$ versus $P = 0.620 \pm 0.08$ respectively (all measures have $P_{\text{uniform}} = 1:\text{million}$ or less except the P measure for round BCGs which has $P_{\text{uniform}} = 1:650$). It is also noticeable that there is a general trend for the same dependency on signal strength to be visible in all three individual radial bins (i.e., compare matching filled symbols within the BCG shape subsamples). The BCG shape is an interesting parameter as more intrinsically elliptical BCGs could form via mergers occurring preferentially from particular directions. Given that the BCG PA shows preferential alignment with the LSS out to many R_{200} from the clusters, this could be interpreted as strong evidence that filaments feed in galaxies to the cluster along their lengths and, in the process, the BCG grows along that direction. We note that if an intrinsically elliptical BCG aligns with the surrounding LSS, projection effects could cause the BCG to appear round on the sky. But this would also cause the LSS to be projected down our line of sight, and thus weaken the coherence signal. Thus, the dependency we see on BCG shape could be partly a result of projection effects, rather than the intrinsic shape of the BCG. Either way, there would be the requirement that there is some genuine alignment in three dimensions between the BCG and the LSS.

- *Nconnect*: Nconnect is the number of connecting filaments at $3 R_{200}$ from the cluster centre. We split our sample into clusters with two, three and four or more connecting filaments (cluster sample sizes of 24, 28 and 39 respectively) in the second column of Figure 2. In the ‘Fiducial’ subsample, no limit on numbers of connecting filaments was imposed. In general we do not see a clear dependency, although there is a hint that Nconnect=3 results in a stronger alignment signal, although it is only clearly significant for the V measure when all the radial bins are combined (0-10 R_{200}). The lack of a strong dependency on Nconnect is interesting. Naively, we might have expected that Nconnect = 2 clusters would be better aligned with their filaments as feeding of galaxies would only be from a single filament passing through the cluster and so occur from less different directions. However we note that, by eye in the LSS maps of individual clusters, even when there are several connections (Nconnect = 3 or Nconnect > 4) to a cluster, they still tend to prefer to connect with the cluster at a similar position-angle. Therefore, feeding of galaxies may still occur from preferential PAs even when there are multiple filaments connected to a cluster.

- *$R_{200,\text{connect}}$* : This parameter controls the radius at which the filaments connect to the cluster. In our fiducial set-up, we chose it to be at $3 R_{200}$ from the cluster. Here, we can see the impact on the alignment signal strength if we choose it to instead be at $1 R_{200}$ from the cluster. For the combined radial bins (0-10 R_{200}), we see a significant increase in the alignment signal strength for all three measurements (U , V and P) if we restrict our cluster sample to clusters with $R_{200,\text{connect}}=1 R_{200}$. This stricter criterion reduces the number of clusters in our sample from 91 to 64, but nevertheless strengthens the alignment signal. For example, comparing clusters with $R_{200,\text{connect}}=3 R_{200}$ versus $R_{200,\text{connect}}=1 R_{200}$, $U = 35.07$ versus $U = 35.83$ (typical errors ~ 0.15), $V = 581.7 \pm 38.9$ versus $V = 684.3 \pm 38.4$, and $P = 0.581 \pm 0.006$ versus $P = 0.597 \pm 0.006$

respectively (where all measurements have $P_{\text{uniform}} = 1:\text{million}$ or less). This result is generally confirmed in the individual radial bins, although with a lower significance than when all the radial bins are combined.

- *Near Pair*: In the ‘Fiducial’ model, we exclude clusters with a nearby pair cluster within $5 R_{200}$, which gives a sample of 91 clusters. Here, we consider the impact of removing this limit (subsample labelled ‘No Limit’, sample size of 124 clusters) or making the criteria much stricter by excluding clusters with a nearby pair within $10 R_{200}$ (sample size of 55 clusters). We note that we use all 211 clusters to identify neighbour clusters. For the combined radial bins, we see that removing the limit reduces signal strength for all three signal strength measures (U , V and P). For both the V and P measures, we see that setting the limit to $5 R_{200}$ results in the alignment signal being the strongest and significantly so.

- *LSS Weight*: We normally use an LSS skeleton obtained from the galaxy distribution and the galaxy luminosity-weighted Delaunay tessellation. Here, we test the effect on the alignment signal of using an LSS skeleton that only depends on galaxy number density (labelled ‘unweighted’ as it is not luminosity weighted). It is noticeable that the alignment signal strength for the combined radial bins (0-10 R_{200}) is significantly increased for all three measures (U , V and P) when luminosity-weighting is used. For example, comparing the non-weighted LSS skeleton versus the weighted LSS skeleton, we measure $U = 34.34$ versus $U = 34.82$ (typical errors ~ 0.23), $V = 314.9 \pm 33.5$ versus $V = 479.5 \pm 34.9$, and $P = 0.548 \pm 0.007$ versus $P = 0.581 \pm 0.007$ respectively (where all measurements have $P_{\text{uniform}} = 1:\text{million}$ or less except the non-weighted LSS measure of U which has $P_{\text{uniform}} = 1:110$ thousand). In general, this result is also seen for the individual radial bins as well, although sometimes with less significance.

- *Dependence on Projected Distance from Cluster*: We note that it is not fair to compare alignment signal strength measurements between radial bins of the above subsamples as, radially, we did not match them in sample size to avoid excessively reducing the number statistics. However, as an additional test, for the Fiducial model only, we match the radial bin sample sizes of LSS segments so as we can see how the signal strength varies with radius, independent of the effects of the changing galaxy numbers with radius. This reduces our statistics significantly, and, for the U measure the results are not significant. But for the V and P measures, the results are significant. We find that the signal strength decreases significantly with increasing projected radius from the cluster for both the V and P measures. For the radial bins (0-3, 3-6, 6-10) R_{200} , $V = (231.8, 200.4, 158.0)$ with typical errors of ~ 20.0 , and $P = (0.603, 0.567, 0.564)$ with typical errors of ~ 0.01 . This suggests that the BCG PA is more strongly aligned with the nearby LSS.

- *Alignment of cluster members versus LSS segments*: We also run an additional test that is not directly shown in Figure 2, comparing the S/N of all the cluster members combined ($R < 3 R_{200}$) with the S/N of all the LSS segments combined ($R < 10 R_{200}$). This test is conducted only for galaxies that are members of clusters in the ‘Cluster Members + LSS’ sample. We find that the alignment signal is stronger in the cluster member population than for the LSS segments. For example, $V=797.8$ ($P=0.596$) for cluster members versus $V=685.97$ ($P=0.581$) for the LSS segments. This result may be consistent with stronger alignment for at shorter projected distances, as the satellite population is both closer and presents a stronger alignment signal. However, it may also be partly because the original selection of our cluster members sample is biased towards redder galaxies which are known to present stronger signals of alignment (for further discussion, see Appendix A).

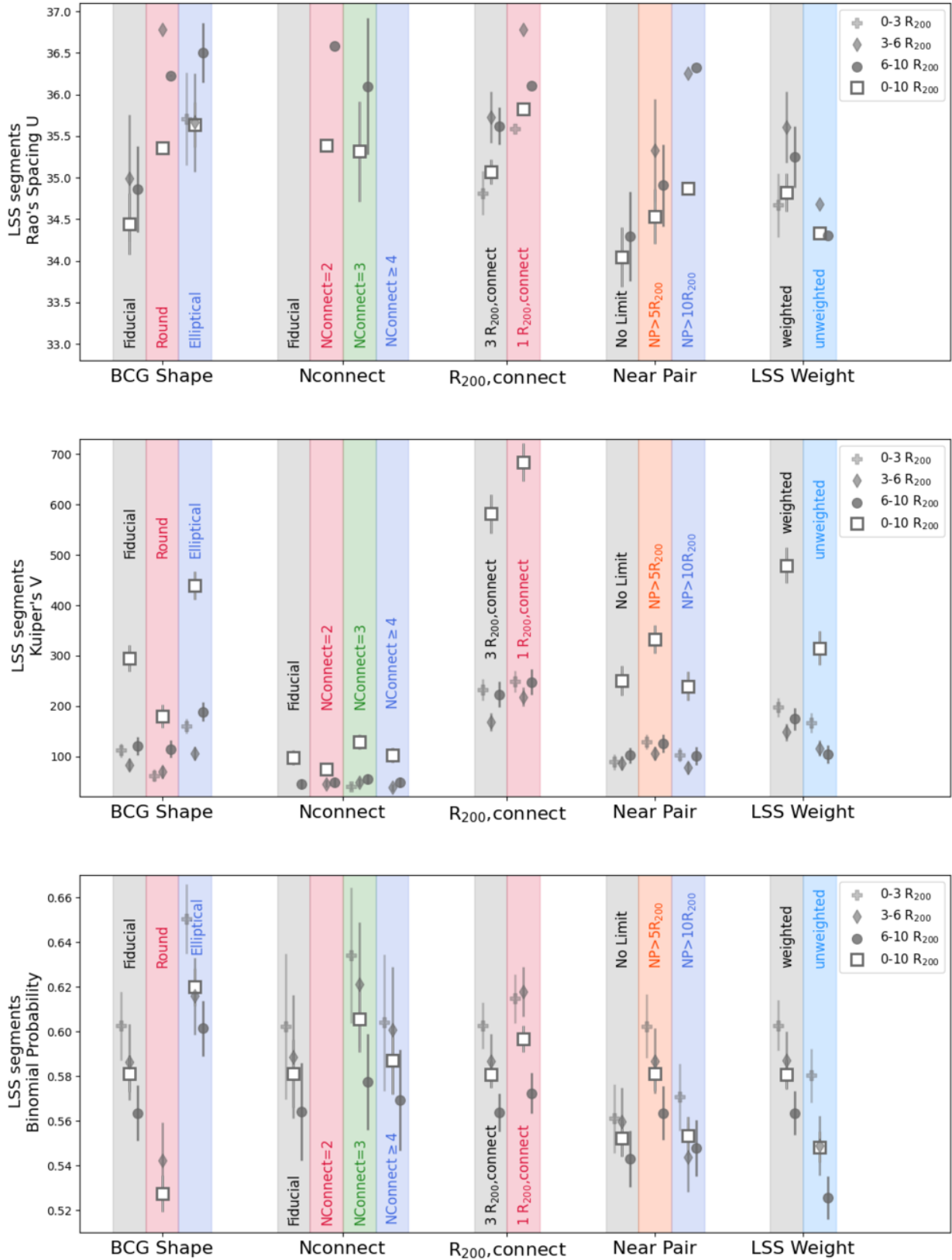


Figure 2. For the ‘Cluster Members + LSS’ sample, comparison of the strength of the alignment signal using equal sample sizes. Symbols indicate the radial bins (see legend; 0 – 3 R_{200} , 3 – 6 R_{200} , 6 – 10 R_{200} , and 0 – 10 R_{200} for all the LSS segments combined). Subsamples (e.g., BCG shape) that can be compared at fixed sample size are grouped together along the x-axis. See text in Section 4.2 for details on each parameter. Please note that sample sizes vary between radial bins, and between subsamples (e.g., between ‘BCG shape’ and ‘Nconnect’). Therefore, comparisons should only be done within a subsample and for the same radial bin.

In summary, for the strength of the signal of alignment between the BCG PA and the positions of LSS segments about the cluster center, the shape of the BCG is a key parameter. Forcing the cluster to be directly connected to the LSS at $1 R_{200}$ and using a luminosity-weighted LSS skeleton both resulted in a significant increase in alignment signal strengths.

4.3 Results of subsampling the ‘Cluster Members only’ sample

We first measure the alignment signal for all of the cluster members combined into a single stack of all 211 clusters. For all the radial bins combined (0-3 R_{vir}), we measure $U=33.6$, $V=1767.5$, and $P=0.57$. The V and P measures are non-uniform at a one in >one million level (very high significance, $>4.8\sigma$) and the same is true for all the individual radial bins (0-1 R_{vir} , 1-2 R_{vir} , and 2-3 R_{vir}). The U measure is less significant compared to the V and P measure. For all radial bins combined, it is non-uniform at a 1:1350 level (3.2σ). For the individual radial bins 0-1 R_{vir} , 1-2 R_{vir} and 2-3 R_{vir} , it is non-uniform at the level 1:400 (2.8σ), 1:25 (1.8σ) and 1:70 (2.2σ) respectively.

Now, we split the ‘Cluster Members only’ sample into subsamples according to the seven different criteria described below. Some of these criteria match those used in Figure 2 (e.g., BCG Shape, Near Pair). But, we now consider some new subsamples that are unrelated to the LSS (e.g., Cluster Mass, member Luminosity, etc).

Once again for clarity, we note that each subsample is of equal size to enable a fair comparison of the measured U , V and P measures, free from the effects of changing subsample size. However, this means that comparisons of alignment signal strength should only be done *within a subsample, and for matching radial bins*. We neglect data points representing samples whose probability to be uniform is too high (i.e., P_{uniform} , as described in Section 3.4), and error bars arising from the subsampling procedure are calculated as described in Section 3.5. The results are shown in Figure 3. Our main sample (labelled ‘All’ in the legends), consists of the full 211 clusters, and more than 13,000 spectroscopically confirmed cluster members.

- *BCG shape*: The BCG shape is classified in the same way as in Section 4.2, creating a sample of 106 (105) elliptical (round) BCGs. As we saw in Section 4.2, there appears to be a visibly stronger alignment signal when we consider clusters with ‘elliptical’ BCGs compared to ‘round’ BCGs (see first column of Figure 3). However, in this case, the alignment is with the cluster members rather than with LSS segments. For satellites in all the radial bins combined (0-3 R_{200}), this is visible for all three measures (U , V and P), and is highly significant for the V and P measures. For example, comparing the clusters with round versus elliptical BCGs, we measure $U = 33.33$ versus $U = 34.33$ (typical errors ~ 0.15), $V = 510.2 \pm 50.5$ versus $V = 1153.3 \pm 53.3$, and $P = 0.541 \pm 0.005$ versus $P = 0.597 \pm 0.005$ respectively (where all measurements have $P_{\text{uniform}} = 1$:million or less except the U measure for round BCGs which has P_{uniform} of only 1:9 and so is excluded from the plot). Similar results are seen in all radial bins, albeit with lowered significance.

- *Cluster Mass*: In the second column of Figure 3, we divide the main sample into a high- and low-mass cluster sample (divided below a cluster mass of $3 \times 10^{14} M_{\odot}$). The cluster sample size is 137 (74) low (high)-mass clusters. Although there are many more low-mass clusters, they also contain less cluster members, therefore the galaxy subsample sizes are more similar in size. We do not see evidence for a significant dependence on cluster mass in these panels in either the combined radial bins or individual radial bins.

- *Cluster Member Luminosity*: In the third column of Figure

- 3, we split the sample into bright ($M_r < -20.5$) and faint ($M_r > -20.5$) cluster member subsamples, using the full 211 clusters. For the combined radial bins only (0-3 R_{200}), there is a hint that more luminous galaxies show slightly stronger alignment signal for U , V and P measures but it is of low significance.

- *Nearby Universe*: In ‘Nearby Universe’ (fourth column) we take a low redshift subsample labelled ‘ $z < 0.1$ ’, containing 108 of the 211 clusters. For the combined radial bins (0-3 R_{200}), the low redshift sample shows consistently higher alignment signal for all three measures (U , V and P) although it is of low significance for the U measure. For example, comparing clusters with no redshift limit versus clusters with redshift < 0.1 , we measure $U = 33.62$ versus $U = 33.77$ (typical errors of ~ 0.20), $V = 982.6 \pm 56.3$ versus $V = 1118.7 \pm 57.1$, and $P = 0.567 \pm 0.004$ versus $P = 0.577 \pm 0.004$ respectively (where all measurements have $P_{\text{uniform}} = 1$:million or less except the U measures which have $P_{\text{uniform}} = 1$:60 and 1:3700 respectively). It is unclear if this represents a true demonstration that the alignment signal is evolving with the age of the Universe. The difference in maximum lookback-time between the ‘All’ and ‘Nearby Universe’ samples is only ~ 2 Gyr, therefore any evolutionary change would have to be very recent. We test the possibility that there might be larger numbers of satellites with measured redshifts in nearby clusters. But, we find little evidence for this or for differences in completeness when we compare the ‘All’ and ‘Nearby Universe’ sample, which gives additional weight to the hypothesis that we may in fact be measuring some true (recent) time evolution in the alignment signal.

- *Near Pair*: Here, we take subsamples based on how close is the nearest cluster (labelled ‘Near Pair’). As with the LSS segments in Section 4.2, for the combined radial bins, there is some evidence for stronger alignment signal when some kind of restriction on the distance to the nearest cluster is included. Although, for the ‘Satellites only’ sample, this result is only significant for the V and P measures. For example, comparing clusters with no limit on nearby clusters versus clusters where the nearest cluster must be more than 5 R_{200} away, we measure $U = 33.62 \pm 0.21$ versus $U = 33.72 \pm 0.18$, $V = 925.1 \pm 58.0$ versus $V = 1116.3 \pm 58.9$, and $P = 0.563 \pm 0.004$ versus $P = 0.576 \pm 0.004$ respectively (where all measurements have $P_{\text{uniform}} = 1$:million or less except the U measures which have $P_{\text{uniform}} = 1$:5). The preference for stronger alignment when the separation must be at least 5 R_{200} (labelled ‘NP>5 R_{200} ’) is less significant than was seen in the ‘Cluster members + LSS’ sample.

- *Cluster Completeness*: Here, we subsample clusters whose total completeness is high (second column from the right, labelled ‘Completeness’). We first measure the average completeness of galaxies within a 6-by-6 R_{200} square, centred on the cluster (i.e., out to a projected radius of $\sim 3 R_{200}$). Those with an average completeness > 0.75 are classified as ‘High’ completeness, and this subsample contains 104 of the 211 clusters. In general, we do not see a strong dependency of alignment signal on this parameter, for any of the alignment measures and across all the different radial bins, perhaps in part due to our efforts to correct the alignment signal for incompleteness (as described in Section 2.3).

- *Minimum Number of Members*: Finally, in the last column, we take a subsample where the number of cluster members must be ≥ 100 . This subsample contains 112 of the 211 clusters. There is a small hint that this restriction may slightly increase the alignment signal for the combined radial bins of the V and P measures only but it is low significance.

- *Dependence on Projected Distance from Cluster*: Similarly to our analysis of the LSS segments in Section 4.2, we now match the radial bin sample sizes to see how the signal strength varies with

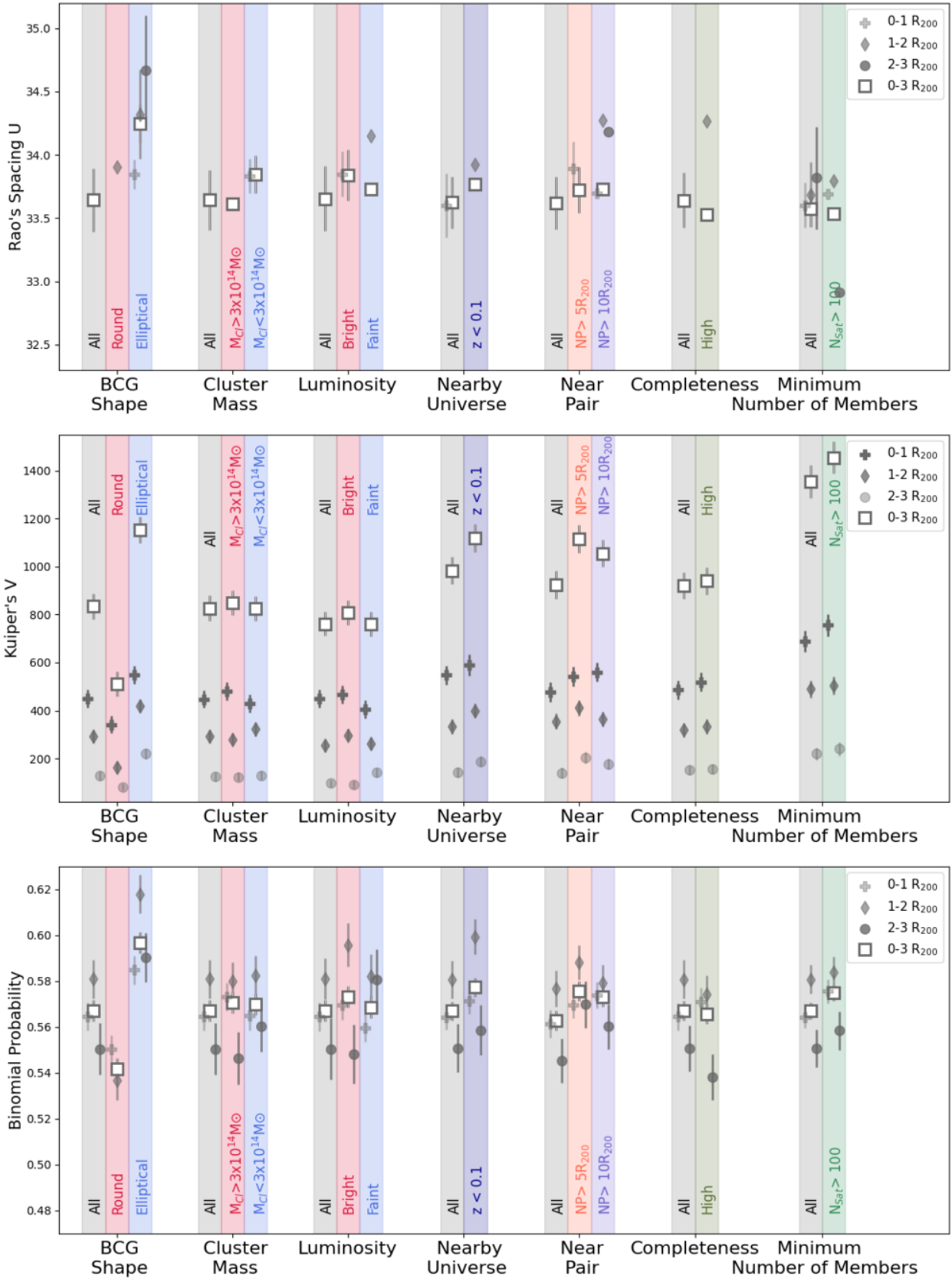


Figure 3. Comparing the alignment signal strength for the ‘Cluster Members-only’ sample. The y-axis is the value of U , V and P measure from top panel to bottom. The data symbols indicate the radial bin (see legend; 0 – 1 R_{200} , 1 – 2 R_{200} , 2 – 3 R_{200} and 0 – 3 R_{200}). Subsamples that can be compared for equal sample size are grouped together along the x-axis. See text in Section 4.3 for a description of each parameter. Please note that sample sizes vary between radial bins, and between subsamples (e.g., between ‘BCG shape’ and ‘Cluster Mass’). Therefore, comparisons should only be done within a subsample and for the same radial bin.
MNRAS **000**, 1–21 (2023)

radius, independent of the effects of changing sample size, for the ‘All’ model only. In contrast to the LSS segments (whose signal decreased with projected radius for both the V and P measures), we do not see a clear trend with projected radius for any of the three measurements of alignment strength. The results for U are not significant. But, for V and P the results are significant and the strongest alignment signal arises in the second radial bin of $1-2 R_{200}$. For the radial bins $(0-1, 1-2, 2-3)R_{200}$, $V = (320.7, 382.6, 274.6)$ with typical errors of ~ 30.0 , and $P = (0.564, 0.581, 0.550)$ with typical errors of ~ 0.007 . This may indicate that the general trend for decreasing alignment signal with radius is reversed near the cluster center, as a result of a greater degree of virialization of those cluster members. Alternatively, galaxies near the cluster center are more likely to have fallen in earlier, when the alignment signal was perhaps less strong.

In summary, for the strength of the alignment signal between the BCG PA and the cluster member locations on the sky out to $3 R_{200}$, the most significant parameter we find is the BCG shape. We see this result across all three measures of alignment signal (U , V and P), and often in multiple radial bins. This strong dependence on BCG shape qualitatively agrees with the results for BCG alignment with the LSS segments in Section 4.2. We also see evidence for increased alignment signal in our low redshift sample across the three measures but with less significance than the dependency on BCG shape. Finally, there is some evidence for an increase in alignment signal strength when clusters with another cluster within $5 R_{200}$ are removed from the sample in the case of the measures V and P .

4.4 Searching for alignment between the isophotal PAs of cluster members and their BCG

In Huang et al. (2018), it was reported that a signal of alignment between a cluster BCG PA and the satellite galaxies PAs exists, although other studies do not find a clear indication of this beyond the second or third brightest galaxy in the cluster (Torlina et al. 2007; Niederste-Ostholt et al. 2010; Sifón et al. 2015; West et al. 2017). We note that this differs from the alignment we have been measuring. In their study they measure the isophotal PAs (rather than the positional PAs on the sky) of the individual cluster members. They found that this type of alignment was stronger for brighter satellites and those closer to the cluster centre. The redshift range of their sample is roughly comparable with ours and consists of relatively nearby clusters ($z < 0.35$).

Inspired by their initiative, we attempted to make the same measurement using our ‘Cluster Members-only’ sample. In Figure 4, we plot histograms of the difference in the PA angle between the BCG and their cluster members isophotal PAs. If there is no alignment, and cluster members have completely random isophotal PAs that are independent of their BCG PA, then we expect a flat distribution. To maximise the statistics, we use our ‘Cluster Members-only’ sample (labelled ‘Full Sample’ in the legend). We see no clear evidence for the cluster members to show any preference for particular isophotal PAs with relation to their BCG PA. Our three statistical measurements of alignment (Rao’s spacing test, Kuiper’s V test, and the Binomial Probability Test) all find the distribution of cluster member isophotal PAs is highly consistent with a uniform distribution.

We also try dividing up the sample into various subsamples. The ‘Nearby Members Only’ subsample is cluster members within $1 R_{200}$ only. We also consider a sample where the cluster members must have an elliptical shape so as the PA should be clearly defined, and where both the cluster members and BCGs must be elliptical (labelled ‘El-

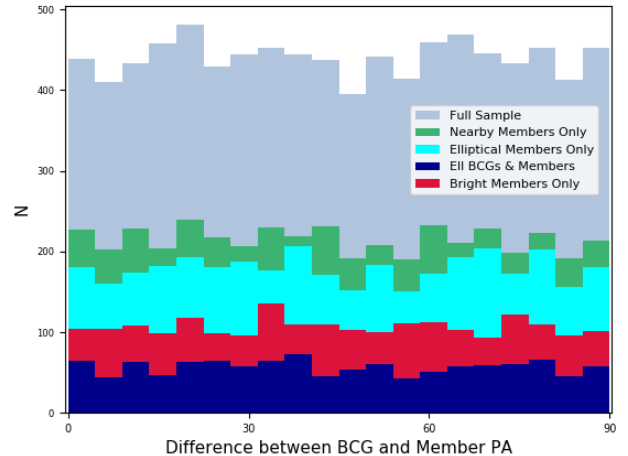


Figure 4. Distribution of the angle between the satellite and BCG PA for the ‘Cluster Members-only’ sample (‘Full Sample’ in the legend). We also show the following subsamples (indicated in the legend); ‘Nearby Members Only’ for cluster members that are within $1 R_{200}$ of the cluster centre, ‘Elliptical Members Only’ and ‘Ell BCGs & Members’ including only galaxies with r-band axial ratio $b/a < 0.75$, and ‘Bright members only’ including only cluster members with $M_r < -20.5$.

lptical Members Only’ and ‘Ell BCGs & Members’, respectively). As defined previously, an elliptical shape means an axial ratio $b/a < 0.75$. Finally, we consider a subsample with only bright cluster members ($M_r < -20.5$; labelled ‘Bright Members only’). In all cases, the cluster member BCGs have flat distributions, as if they are randomly orientated with respect to their BCG. Measurements of the U , V and P values give probabilities of being uniform that are too high to pass our criteria for significance as described in Section 3.4 (e.g., For the P measure, $P_{\text{uniform}} > 0.93$ for the ‘Full sample’, meaning it is highly probable to be consistent with a uniform distribution).

Although we see no clear evidence for cluster-satellite isophotal PA alignment in our data set, we note that our statistics are poorer than in the Huang et al. (2018) study. We have only 211 clusters compared to their several thousands of clusters, and our satellite sample is roughly one-tenth the size of their sample. Nevertheless, our spectroscopy is deeper, and we only used spectroscopically confirmed cluster members, meaning our membership criteria is more strict and accurate. Thus, our sample could potentially provide an interesting data set for this experiment. It is interesting that we cannot detect this type of BCG-satellite isophotal PA alignment, and yet we detect such significant signals of BCG alignment with the positions of the cluster members and the LSS about the cluster within the same sample. We conclude that this is a clear demonstration of how much stronger the alignment signal is with positions of the cluster members and the LSS compared to the isophotal PA alignment between BCG and satellites.

5 DISCUSSION AND SUMMARY

Using a sample of 211 clusters whose cluster members have been determined using deep spectroscopy, we search for a well-known signal of alignment between the position angle (PA) of the Brightest Cluster Galaxy (BCG) and the locations of the cluster members on the sky about the cluster centre (referred to as ‘BCG-cluster’ alignment).

The deep spectroscopy provides us with large numbers of cluster members in each cluster (typically > 100 members) which should make our sample ideal to detect alignment signals. Furthermore, using the overlap with Sloan Digital Sky Survey (SDSS) imaging, we can make corrections for incompleteness to reduce the possibility that the measured alignment is not artificially a result of uneven completeness levels about the cluster centers.

We combine this data set with a 3D map of the skeleton of the Large Scale Structure (LSS) derived using SDSS data. This allows us to search for a direct link between the BCG PA and the location of the LSS segments on the sky at distances far beyond the cluster members. By using the skeleton of the LSS, we effectively filter out noise from scatter in individual galaxy positions in the distribution of the LSS. We also remove filaments that are not interconnected with the main filaments that directly connect to the cluster of interest. As a result, we should be more sensitive to any signal of alignment and we use this data set to search for alignment signal out to projected radii as large as $6 - 10 R_{200}$.

BCG alignment is measured using three individual statistical measures; Rao's spacing test, Kuiper's V-statistic, and the Binomial probability (denoted as the measures U , V and P respectively). We test the non-uniformity of a measurement by computing the probability that the measure is reproduced by randomly sampling PAs from a uniform distribution with a sample of equal size to the observed sample.

We also divide our sample up into subsamples according to a wide range of parameters, to try to measure the dependency of the alignment strength on those parameters. When comparing the strength of the alignment signal between subsamples, we match the size of the subsamples to avoid variations in signal strength due to differing sample size.

Our key results are given in the following:

(i) The BCG alignment signal for a stack of all the LSS segments available is very high significance (1: $>$ million chance of being drawn from a uniform distribution) for the U , V and P measure. This is true in all of the individual bins of projected radius as well, including our most distant at $6-10 R_{200}$ from the cluster centre⁴.

(ii) The shape of the cluster BCG is a key parameter determining the strength of the alignment signal. BCGs that appear more elliptical show significantly stronger alignment with both their cluster members and also with the surrounding LSS segments. When all radial bins are combined, this is visible for all three measures of the alignment signal (U , V and P), and is generally visible in the individual projected radial bins as well, even at $6-10 R_{200}$ from the cluster centre.

(iii) The BCG alignment signal with the LSS segments increases significantly when we require that a filament connects with the cluster at $1 R_{200}$ instead of $3 R_{200}$, and also when we use a luminosity-weighted LSS skeleton instead of simply the number density of galaxies. The alignment signal appears stronger for two of our measures (V and P) when we remove clusters from the sample with a nearby companion cluster, and this holds true for BCG alignment with both the cluster members and LSS segments. There is also a hint that clusters connected with three or more filaments have slightly stronger alignment signal but it is a low-significance result.

(iv) For the BCG alignment with the members of the cluster, the alignment signal increases for two of our measures (V and P) when we consider a low redshift subsample ($z < 0.1$) although the significance is not as high as seen for other parameters mentioned

above. Meanwhile, we see no clear dependency (or only a weak, low-significance dependency) on parameters such as the cluster mass or galaxy luminosity.

The fact that the BCG tends to be preferentially aligned with LSS at projected distances as large as $6 - 10 R_{200}$ is telling. So called 'backsplash' galaxies (galaxies that have previously entered a sphere of radius $1 R_{200}$ from the cluster but are now found at larger radius; Gill et al. 2005) typically don't reach further than $\sim 2-3 R_{200}$ from the cluster centre. Therefore, we physically interpret our results as evidence that the preferential feeding of galaxies into clusters along connected filaments must build-up the cluster BCG. And, this process must continue throughout the time period when a significant fraction of the BCG stars were put in place. If the merger-axis is preferentially aligned with the filaments, the stellar body of the BCG may become extended in that same direction, and growth could potentially occur through a combination of minor and major mergers. Similarly, the galaxies that are fed into the clusters but don't merge with the BCG will tend to form a population of cluster members that are similarly extended along the direction of the filaments. We note that the continuous feeding of new material into the cluster, along the preferential directions of filaments, would be expected to eventually change the shape of the main cluster dark matter halo itself, if the new mass is a significant fraction of the total.

Finally, we also search for evidence that the PAs of the cluster members (based on their shape) might be aligned with their BCG PA (e.g. Huang et al. 2018). However, we find no clear evidence for this in our sample, and our results are consistent with the PAs of the cluster member being randomly orientated with respect to the PA of their BCG. This demonstrates how much weaker this type of alignment is compared to the BCG-cluster and BCG-LSS alignment.

If mergers along preferential directions are indeed responsible for the clear alignment we see between the PA of the BCG and the locations of cluster members and the LSS skeleton, it is interesting to ask if we might expect a dependency of the alignment signal strength on the cluster dynamical state. We plan to present the results of such an analysis in a following paper, where we will separate the cluster sample according to their dynamical state and quantify the strength of the alignment with the cluster members and surrounding LSS.

ACKNOWLEDGEMENTS

We thank the referee for a careful reading of the draft and constructive comments that improved the paper. We thank Stéphane Rouberol for the smooth running of the HORIZON Cluster, where some of the post-processing was carried out. We thank Thierry Sousbie for provision of the DisPerSE code (ascl.net/1302.015). R.S. acknowledges support from Fondecyt Regular Grant project number 1230441. J.Y. was supported by a KIAS Individual Grant (QP089901) via the Quantum Universe Center at Korea Institute for Advanced Study. J.W.K. acknowledges support from the National Research Foundation of Korea (NRF), grant No. NRF-2019R1C1C1002796, funded by the Korean government (MSIT). H.S.H. was supported by the National Research Foundation of Korea (NRF) grant funded by the Korea government (MSIT) (No. 2021R1A2C1094577). K.K. acknowledges support from the DEEPDIP project (ANR-19-CE31-0023). Funding for the Sloan Digital Sky Survey IV has been provided by the Alfred P. Sloan Foundation, the U.S. Department of Energy Office of Science, and the Participating Institutions. SDSS-IV acknowledges support and resources from the Center for High Performance Computing at the University of Utah. The SDSS website is www.sdss.org. SDSS-IV is managed by the Astrophysical Research Consortium for

⁴ with the sole exception of the innermost radial bin of the U measure which has 1: $>$ 100 thousand chance of being uniform

the Participating Institutions of the SDSS Collaboration including the Brazilian Participation Group, the Carnegie Institution for Science, Carnegie Mellon University, Center for Astrophysics | Harvard & Smithsonian, the Chilean Participation Group, the French Participation Group, Instituto de Astrofísica de Canarias, The Johns Hopkins University, Kavli Institute for the Physics and Mathematics of the Universe (IPMU) / University of Tokyo, the Korean Participation Group, Lawrence Berkeley National Laboratory, Leibniz Institut für Astrophysik Potsdam (AIP), Max-Planck-Institut für Astronomie (MPIA Heidelberg), Max-Planck-Institut für Astrophysik (MPA Garching), Max-Planck-Institut für Extraterrestrische Physik (MPE), National Astronomical Observatories of China, New Mexico State University, New York University, University of Notre Dame, Observatório Nacional / MCTI, The Ohio State University, Pennsylvania State University, Shanghai Astronomical Observatory, United Kingdom Participation Group, Universidad Nacional Autónoma de México, University of Arizona, University of Colorado Boulder, University of Oxford, University of Portsmouth, University of Utah, University of Virginia, University of Washington, University of Wisconsin, Vanderbilt University, and Yale University.

DATA AVAILABILITY

The data underlying this article will be shared on reasonable request to the corresponding author.

REFERENCES

- Abazajian K. N., et al., 2009, *ApJS*, **182**, 543
 Ahumada R., et al., 2020, *ApJS*, **249**, 3
 Argyres P. C., Groth E. J., Peebles P. J. E., Struble M. F., 1986, *AJ*, **91**, 471
 Catelan P., Theuns T., 1996, *MNRAS*, **282**, 455
 Codis S., Jindal A., Chisari N. E., Vibert D., Dubois Y., Pichon C., Devriendt J., 2018, *MNRAS*, **481**, 4753
 Darragh Ford E., et al., 2019, *MNRAS*, **489**, 5695
 Diaferio A., 1999, *MNRAS*, **309**, 610
 Donahue M., et al., 2016, *ApJ*, **819**, 36
 Einasto M., et al., 2020, *A&A*, **641**, A172
 Einasto M., et al., 2021, arXiv e-prints, p. [arXiv:2103.02326](https://arxiv.org/abs/2103.02326)
 Faltenbacher A., Jing Y. P., Li C., Mao S., Mo H. J., Pasquali A., van den Bosch F. C., 2008, *ApJ*, **675**, 146
 Georgiou C., et al., 2019, *A&A*, **622**, A90
 Gill S. P. D., Knebe A., Gibson B. K., 2005, *MNRAS*, **356**, 1327
 Gladders M. D., Yee H. K. C., 2000, *AJ*, **120**, 2148
 Gouin C., Bonnaire T., Aghanim N., 2021, arXiv e-prints, p. [arXiv:2101.04686](https://arxiv.org/abs/2101.04686)
 Hao J., Kubo J. M., Feldmann R., Annis J., Johnston D. E., Lin H., McKay T. A., 2011, *ApJ*, **740**, 39
 Huang H.-J., Mandelbaum R., Freeman P. E., Chen Y.-C., Rozo E., Rykoff E., Baxter E. J., 2016, *MNRAS*, **463**, 222
 Huang H.-J., Mandelbaum R., Freeman P. E., Chen Y.-C., Rozo E., Rykoff E., 2018, *MNRAS*, **474**, 4772
 Hwang H. S., Geller M. J., Diaferio A., Rines K. J., Zahid H. J., 2014, *ApJ*, **797**, 106
 Hwang H. S., et al., 2016, *ApJ*, **818**, 173
 Kraljic K., et al., 2018, *MNRAS*, **474**, 547
 Kraljic K., et al., 2020, *MNRAS*, **491**, 4294
 Lambas D. G., Groth E. J., Peebles P. J. E., 1988, *AJ*, **95**, 996
 Libeskind N. I., Hoffman Y., Forero-Romero J., Gottlöber S., Knebe A., Steinmetz M., Klypin A., 2013, *MNRAS*, **428**, 2489
 Moretti A., et al., 2017, *A&A*, **599**, A81
 Niederste-Ostholt M., Strauss M. A., Dong F., Koester B. P., McKay T. A., 2010, *MNRAS*, **405**, 2023
 Paz D. J., Sgró M. A., Merchán M., Padilla N., 2011, *MNRAS*, **414**, 2029
 Ragone-Figueroa C., Plionis M., 2007, *MNRAS*, **377**, 1785
 Ragone-Figueroa C., Granato G. L., Borgani S., De Propriis R., García Lambas D., Murante G., Rasia E., West M., 2020, *MNRAS*, **495**, 2436
 Rines K., Diaferio A., 2006, *AJ*, **132**, 1275
 Rines K., Geller M. J., Diaferio A., Kurtz M. J., 2013, *ApJ*, **767**, 15
 Rines K. J., Geller M. J., Diaferio A., Hwang H. S., 2016, *ApJ*, **819**, 63
 Rines K. J., Geller M. J., Diaferio A., Hwang H. S., Sohn J., 2018, *ApJ*, **862**, 172
 Rodriguez F., Merchán M., Artale M. C., 2022, *MNRAS*, **514**, 1077
 Rykoff E. S., et al., 2014, *ApJ*, **785**, 104
 Sastry G. N., 1968, *PASP*, **80**, 252
 Sifón C., Hoekstra H., Cacciato M., Viola M., Köhlinger F., van der Burg R. F. J., Sand D. J., Graham M. L., 2015, *A&A*, **575**, A48
 Song H., Hwang H. S., Park C., Smith R., Einasto M., 2018, *ApJ*, **869**, 124
 Sousbie T., 2011, *MNRAS*, **414**, 350
 Sousbie T., Pichon C., Kawahara H., 2011, *MNRAS*, **414**, 384
 Stoughton C., et al., 2002, *AJ*, **123**, 485
 Strauss M. A., et al., 2002, *AJ*, **124**, 1810
 Tegmark M., et al., 2004, *ApJ*, **606**, 702
 Tempel E., et al., 2014, *A&A*, **566**, A1
 Torlina L., De Propriis R., West M. J., 2007, *ApJ*, **660**, L97
 Voges W., et al., 1999, *A&A*, **349**, 389
 Wang P., Luo Y., Kang X., Libeskind N. I., Wang L., Zhang Y., Tempel E., Guo Q., 2018, *ApJ*, **859**, 115
 Welker C., Dubois Y., Pichon C., Devriendt J., Chisari N. E., 2018, *A&A*, **613**, A4
 West M. J., 1994, *MNRAS*, **268**, 79
 West M. J., de Propriis R., Bremer M. N., Phillipps S., 2017, *Nature Astronomy*, **1**, 0157
 Winkel N., Pasquali A., Kraljic K., Smith R., Gallazzi A., Jackson T. M., 2021, *MNRAS*, **505**, 4920
 Wittman D., Foote D., Golovich N., 2019, *ApJ*, **874**, 84
 York D. G., et al., 2000, *AJ*, **120**, 1579
 Yuan Z. S., Wen Z. L., 2022, *MNRAS*, **516**, 3159

APPENDIX A: ADDITIONAL COMPLETENESS TESTS

In Figure A1, we plot the completeness (shown in the colour-bar) of all the galaxies in the ‘Cluster Members only’ sample. On the x-axis they are plotted as a function of r-band petrosian magnitude. In the bottom panel, the y-axis shows the projected distance from the cluster centre normalised by R_{200} . The completeness can be seen to decrease with projected distance. For example, at a magnitude of $r=15$, completeness falls from ~ 1.0 to ~ 0.8 at $3 R_{pr}/R_{200}$ (see also the side panel where we marginalise over the galaxy magnitude). Nevertheless, by measuring the completeness in a grid with cell side lengths of $1 R_{200}$ surrounding the cluster, and then correcting for incompleteness, we have already normalised out this radial dependency in our analysis.

In any case, the existence of a radial gradient should not influence our main conclusions unless it would preferentially affected galaxies in a particular direction with respect to the position angle of the cluster BCG. We see no evidence that the completeness varies as a function of angle from the BCG position angle in our two main samples. An example of this is shown in the top-right panel of Figure 1. In the bottom subpanel, we plot the completeness as a function of angle from the BCG position angle. There is a different line for each radial bin, but they are all nearly horizontal when plotted against the BCG position angle. There is also no evidence that they show higher completeness nearer the BCG position angle, something that would be necessary to artificially induce an alignment signal. We also plot histograms of the number of galaxies in angular bins about the BCG position angle for the ‘Cluster Members + LSS’ sample (different panels are different radial bins). The solid lines are before

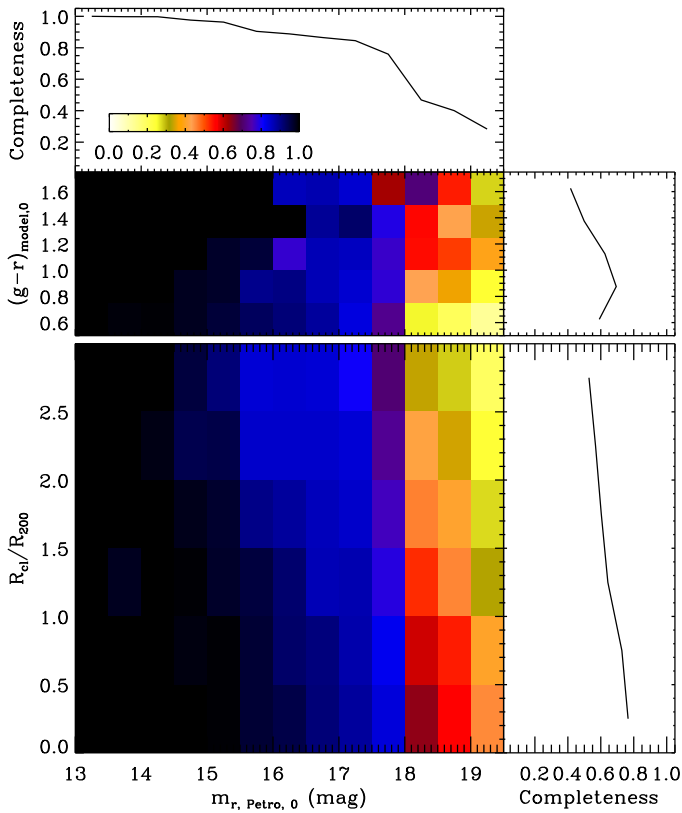


Figure A1. Spectroscopic completeness as a function of a galaxy’s Petrosian magnitude in the r-band (x-axis), (g-r) colour (y-axis, upper panel) and clustercentric radius normalised by R_{200} (y-axis, lower panel) for the full sample of clusters. From top to bottom, the side panels show curves of completeness versus r-band magnitude, versus colour, and versus normalised clustercentric radius. For the (g-r) colour, ‘model’ magnitudes are used (instead of Petrosian magnitudes) to ensure equivalent apertures in both filters.

the completeness correction and the filled histograms are after the completeness correction, and both the histograms show a similar alignment signal. Thus, we expect that our results would not differ strongly, even if we had not conducted our completeness correction.

In the top panel of Figure A1, the (g-r) galaxy colour is shown on the y-axis. The side panel shows that the completeness peaks at (g-r)~0.9. This is to be expected as the cluster galaxies selected from the various HeCS surveys were primarily red sequence selected (Gladders & Yee 2000) based on SDSS panchromatic photometry. Naturally this means the sample is biased towards early-type galaxies. Several previous studies have demonstrated that the signal of alignment is stronger in red galaxies (Rykoff et al. 2014; Georgiou et al. 2019, etc), perhaps because galaxies become preferentially redder towards the centres of cosmological filaments (Kraljic et al. 2018; Winkel et al. 2021). Therefore, we would expect that our sample would be even more sensitive to the alignment signal between cluster members and the BCG position angle. However, we note that we used galaxy redshifts from the SDSS survey to build the skeletons of the LSS. These were not red sequence selected, therefore, unlike the cluster members, the alignment signal between the BCG position angle and positions of filament segments on the sky should not be colour biased in the same manner. Thus, caution is required when directly comparing the alignment signal strength between the cluster members versus the LSS, as noted in Section 4.2.

As a final note on completeness, we also measured an overall completeness for each cluster individually. This is the average completeness of galaxies within a 6-by-6 R_{200} square, centered on the cluster. Those with an average completeness >0.75 were subsampled and classified as ‘high’ completeness. In Figure 3, we test how the relative strength of the alignment signal between the ‘All’ sample and ‘high’ completeness sample varies. We see no clear dependency on the cluster completeness for any of our three measures of the alignment signal, or in any of the subsamples by radial bin range that we consider.

APPENDIX B: TABLE WITH FULL SAMPLE OF CLUSTERS CONSIDERED IN THIS STUDY

A complete list of the clusters considered in this study is provided in Table B1. The ‘Cluster Members only’ sample combines all these clusters. The ‘Cluster Members + LSS’ sample uses only clusters labelled as ‘LSS’ in column (xvi) of the Table. A description of each individual column of the Table follows. Further details can be found in Section 2. Column (i) gives the cluster name. Column (ii)-(iii) are the right ascension and declination of each cluster, as provided by their respective survey. The Table is ordered by increasing right ascension. Column (iv) is the mean redshift of the cluster members, as identified using the caustic technique (Diaferio 1999). Columns (v)-(vii) are cluster mass, velocity dispersion, and R_{200} . Column (viii) shows the r-band apparent magnitude limit that was used for the cluster satellites. Column (ix) is the number of spectroscopically confirmed cluster members. Column (x) is the spectroscopic survey from which the cluster members were selected. Columns (xi-xv) are the properties of the cluster BCG, right ascension, declination, ellipticity, position-angle and r-band absolute magnitude. Finally, column (xvi) indicates if the cluster is located in the main SDSS area where we have built skeletons of the surrounding Large Scale Structure (LSS).

Table B1: Full list of clusters considered. Columns described in Appendix B text

(i) Name	(ii) RA (deg)	(iii) Dec (deg)	(iv) z	(v) Log(M_{200}) $M_{200}(M_{\odot})$	(vi) σ (km/s)	(vii) R_{200} (Mpc)	(viii) r-mag $_{lim}$ (apparent)	(ix) N_{mem}	(x) Survey	(xi) RA_{bcg} (deg)	(xii) Dec_{bcg} (deg)	(xiii) Ellip $_{bcg}$	(xiv) PA_{bcg} (deg)	(xv) r-mag $_{bcg}$ (absolute)	(xvi) LSSflag
RMJ000158d5p120358d0	0.507	12.076	0.201	14.38	647	0.95	19.5	53	HeCS-red	0.494	12.066	0.71	55.2	-23.54	no LSS
A7	2.935	32.417	0.103	14.44	783	1.03	19.5	179	HeCS-SZ	2.939	32.416	0.96	43.3	-22.78	no LSS
A21	5.171	28.675	0.095	14.47	761	1.05	19.5	194	HeCS-SZ	5.155	28.659	0.68	153.8	-24.03	no LSS
RMJ002224d7p231733d0	5.599	23.292	0.137	14.55	710	1.1	19.5	159	HeCS-red	5.615	23.233	0.86	39.0	-22.61	no LSS
A76	10.002	6.818	0.04	14.08	455	0.79	17.77	53	HeCS-SZ	9.86	6.734	0.93	73.0	-22.95	no LSS
RMJ004118d5p252609d1	10.319	25.431	0.145	14.35	652	0.94	19.5	159	HeCS-red	10.327	25.436	0.78	92.8	-23.37	no LSS
A85	10.426	-9.426	0.056	14.4	692	1.02	17.77	217	CIRS	10.429	-9.439	0.73	131.4	-22.48	no LSS
A98S	11.615	20.386	0.104	14.34	594	0.95	19.5	132	HeCS-SZ	11.622	20.468	0.83	72.1	-23.3	no LSS
RMJ005105d2p261716d7	12.763	26.3	0.245	14.47	661	1.0	19.5	92	HeCS-red	12.772	26.288	0.9	115.8	-23.54	no LSS
A0115	14.002	26.34	0.192	15.03	1176	1.56	19.5	87	HeCS-red	14.001	26.342	0.97	45.9	-23.06	no LSS
A119	14.034	-1.164	0.045	14.25	589	0.91	17.77	287	CIRS	14.067	-1.255	0.8	36.7	-23.39	no LSS
RMJ010819d0p275802d1	17.08	27.968	0.239	14.19	609	0.81	19.5	39	HeCS-red	17.079	27.967	0.71	77.3	-22.37	no LSS
A160	18.251	15.496	0.043	13.83	489	0.67	17.77	57	CIRS	18.315	15.516	0.86	-39.5	-22.59	no LSS
A168	18.814	0.264	0.045	14.31	577	0.95	17.77	178	CIRS	18.74	0.431	0.88	155.6	-22.91	no LSS
A193	21.266	8.688	0.048	14.13	658	0.82	17.77	65	HeCS-SZ	21.282	8.699	0.92	133.5	-22.51	no LSS
RXJ0137	24.354	-9.273	0.041	13.94	392	0.72	17.77	78	CIRS	24.314	-9.198	0.73	163.9	-22.62	no LSS
A267	28.176	1.013	0.229	14.69	972	1.19	19.5	91	HeCS	28.175	1.007	0.52	15.8	-24.25	no LSS
A295	30.528	-1.072	0.042	13.56	298	0.54	17.77	52	CIRS	30.572	-1.128	0.74	61.7	-22.76	no LSS
A311	32.379	19.769	0.066	13.76	305	0.62	19.5	50	HeCS-SZ	32.368	19.777	0.63	23.6	-23.55	no LSS
A329	33.671	-4.563	0.139	14.35	641	0.95	19.5	87	HeCS-SZ	33.671	-4.567	0.48	160.7	-23.51	no LSS
A344	35.355	21.348	0.17	14.31	689	0.91	19.5	109	HeCS-SZ	35.391	21.366	0.85	20.0	-23.5	no LSS
RMJ023054d9p024719d6	37.726	2.788	0.243	14.64	878	1.14	19.5	46	HeCS-red	37.729	2.789	0.53	143.0	-24.22	no LSS
A383	42.014	-3.529	0.189	14.71	931	1.22	19.5	145	nonHeCS	42.014	-3.529	0.83	13.7	-23.39	no LSS
RMJ02705d2p384613d4	111.778	38.801	0.208	14.37	614	0.94	19.5	69	HeCS-red	111.772	38.77	0.98	3.7	-22.69	no LSS
RMJ02729d3p422756d1	111.884	42.51	0.183	14.48	702	1.03	19.5	131	HeCS-red	111.871	42.559	0.99	77.6	-23.0	LSS
A586	113.092	31.63	0.17	14.61	779	1.14	19.5	131	HeCS-SZ	113.085	31.689	0.79	-14.3	-22.43	LSS
RMJ03720d9p351741d7	114.335	35.285	0.211	14.45	602	0.99	19.5	96	HeCS-red	114.337	35.295	0.73	8.4	-23.06	no LSS
RMJ075100d8p173753d8	117.815	17.657	0.186	14.24	637	0.85	19.5	111	HeCS-red	117.822	17.66	0.87	94.2	-22.8	LSS
A602	118.506	29.285	0.061	14.64	712	1.23	17.77	85	CIRS	118.319	29.401	0.71	-27.5	-22.22	LSS
RMJ075655d8p383933d2	119.263	38.683	0.217	14.3	683	0.89	19.5	95	HeCS-red	119.232	38.659	0.66	32.8	-22.96	no LSS
RMJ075822d7p264120d6	119.626	26.681	0.23	14.88	986	1.37	19.5	68	HeCS-red	119.621	26.664	0.69	-34.3	-23.13	no LSS
Zw1478	119.919	53.999	0.103	13.82	479	0.64	19.5	65	HeCS	119.919	54.006	0.8	81.9	-23.37	LSS
A611	120.237	36.057	0.287	14.77	883	1.24	19.5	80	nonHeCS	120.237	36.057	0.7	41.4	-23.69	no LSS
A0620	121.435	45.68	0.132	14.41	702	0.99	19.5	144	HeCS-red	121.43	45.683	0.59	-9.6	-22.89	LSS
A646	125.547	47.1	0.127	14.39	653	0.98	19.5	66	HeCS	125.54	47.098	0.58	56.3	-22.81	LSS
Zw1665	125.831	4.382	0.03	13.81	463	0.65	17.77	46	CIRS	125.84	4.372	0.79	144.2	-22.82	LSS
A0657	125.832	15.959	0.152	14.48	777	1.04	19.5	157	HeCS-red	125.83	15.963	0.89	117.5	-23.04	LSS
A655	126.361	47.132	0.127	14.52	777	1.08	19.5	244	HeCS	126.371	47.134	0.75	114.4	-24.12	LSS
A625	126.436	82.31	0.197	13.94	472	0.68	19.5	56	HeCS-SZ	126.462	82.305	0.87	63.1	-22.94	no LSS
RMJ082657d6p310804d9	126.73	31.144	0.209	14.78	890	1.29	19.5	91	HeCS-red	126.74	31.135	0.53	-20.3	-24.22	no LSS
A667	127.019	44.764	0.145	14.46	645	1.02	19.5	139	HeCS	127.024	44.767	0.89	84.0	-23.23	LSS

Table B1: Full list of clusters considered. Columns described in Appendix B text

(i) Name	(ii) RA (deg)	(iii) Dec (deg)	(iv) z	(v) Log(M_{200}) (M_{\odot})	(vi) σ (km/s)	(vii) R_{200} (Mpc)	(viii) r-mag _{lim} (apparent)	(ix) N_{mem}	(x) Survey	(xi) RA _{bcg} (deg)	(xii) Dec _{bcg} (deg)	(xiii) Ellip _{bcg}	(xiv) PA _{bcg} (deg)	(xv) r-mag _{bcg} (absolute)	(xvi) LSSflag
A671	127.133	30.395	0.05	14.51	854	1.12	17.77	130	CIRS	127.132	30.431	0.77	30.3	-23.63	LSS
RMJ083056d4p322412d2	127.691	32.456	0.255	13.94	482	0.67	19.5	32	HeCS-red	127.664	32.453	0.79	76.2	-22.84	no LSS
RMJ083513d0p204654d9	128.76	20.781	0.177	14.35	611	0.93	19.5	105	HeCS-red	128.777	20.829	0.83	112.7	-21.86	LSS
A689	129.356	14.983	0.279	14.19	589	0.8	19.5	70	HeCS	129.352	14.973	1.0	45.4	-23.31	no LSS
A697	130.736	36.362	0.281	14.65	1002	1.13	19.5	88	HeCS	130.74	36.367	0.81	-14.1	-23.36	no LSS
A743	136.614	10.345	0.135	13.74	358	0.59	17.77	20	HeCS-SZ	136.607	10.364	0.75	18.9	-23.04	LSS
A736	136.857	52.115	0.061	13.65	320	0.57	17.77	51	HeCS-SZ	136.945	52.072	0.46	55.5	-22.35	LSS
A750	137.247	11.044	0.164	14.42	681	0.99	19.5	238	HeCS	137.217	11.026	0.5	121.2	-23.83	LSS
MS0906	137.283	10.993	0.177	14.17	664	0.81	19.5	95	HeCS	137.303	10.975	0.66	68.3	-23.68	no LSS
A757	138.077	47.713	0.051	13.56	347	0.54	17.77	52	CIRS	138.009	47.763	0.8	113.6	-21.88	LSS
A773	139.462	51.725	0.217	14.89	1110	1.4	19.5	121	HeCS	139.473	51.727	0.8	88.6	-24.1	no LSS
A779	139.938	33.68	0.023	14.26	528	0.92	17.77	105	CIRS	139.945	33.75	0.75	-22.8	-22.84	LSS
A795	141.024	14.168	0.137	14.55	778	1.1	19.5	170	HeCS	141.064	14.128	0.78	73.9	-22.61	LSS
Zw2701	148.198	51.891	0.216	14.26	652	0.86	19.5	49	HeCS	148.205	51.885	0.62	137.8	-23.94	no LSS
A957	153.425	-0.89	0.046	14.2	763	0.88	17.77	68	CIRS	153.409	-0.925	0.87	95.1	-23.44	LSS
A954	153.437	-0.109	0.093	13.77	510	0.63	17.77	16	CIRS	153.496	-0.082	0.58	122.6	-22.83	no LSS
A961	154.094	33.635	0.127	14.37	725	0.97	19.5	130	HeCS-SZ	154.095	33.638	0.68	63.5	-23.39	LSS
A963	154.26	39.048	0.204	14.6	956	1.12	19.5	193	HeCS	154.265	39.047	0.66	3.9	-23.9	no LSS
A971	154.957	40.99	0.092	14.65	784	1.24	17.77	59	CIRS	154.967	40.988	0.78	87.5	-22.98	LSS
RXCJ1022.0+3830	155.591	38.513	0.055	14.04	573	0.78	17.77	79	CIRS	155.656	38.579	0.74	72.0	-22.92	LSS
A980	155.628	50.102	0.156	14.65	1033	1.18	19.5	193	HeCS	155.618	50.106	0.67	47.9	-23.77	LSS
Zw3146	155.912	4.187	0.289	14.49	858	1.0	19.5	31	HeCS	155.915	4.186	0.66	128.3	-23.56	no LSS
A990	155.912	49.145	0.142	14.18	655	0.83	19.5	94	HeCS	155.916	49.144	0.74	80.7	-23.41	LSS
Zw3179	156.484	12.691	0.142	13.83	541	0.63	19.5	64	HeCS	156.492	12.686	0.57	166.1	-24.37	LSS
A1033	157.932	35.058	0.122	14.45	677	1.03	19.5	144	HeCS	157.935	35.041	0.64	24.7	-23.01	LSS
A1035B	158.031	40.306	0.08	14.1	640	0.81	17.77	27	CIRS	158.058	40.271	0.89	-11.9	-23.23	no LSS
A1035A	158.121	40.152	0.068	14.34	536	0.98	17.77	64	CIRS	158.098	40.169	0.91	80.6	-22.16	LSS
A1066	159.887	5.175	0.068	14.67	771	1.26	17.77	161	CIRS	159.778	5.21	0.62	138.0	-22.33	LSS
A1068	160.187	39.951	0.139	14.92	1028	1.47	19.5	123	HeCS	160.185	39.953	0.58	128.9	-23.8	LSS
A1126	163.49	16.85	0.085	14.13	565	0.81	17.77	64	KYDISC	163.461	16.85	0.76	105.3	-24.16	LSS
RXJ1053.7+5450	163.531	54.82	0.073	14.54	605	1.14	17.77	130	CIRS	163.402	54.868	0.94	17.7	-22.21	LSS
A1132	164.616	56.782	0.135	14.55	749	1.1	19.5	163	HeCS	164.599	56.795	0.77	87.4	-23.63	LSS
A1142	165.239	10.548	0.035	14.34	579	0.98	17.77	92	CIRS	165.239	10.505	0.96	158.4	-22.51	LSS
A1173	167.304	41.556	0.076	13.98	598	0.74	17.77	18	CIRS	167.314	41.561	0.95	131.8	-23.33	LSS
A1185	167.695	28.706	0.034	14.33	633	0.96	17.77	226	HeCS-SZ	167.662	28.769	0.88	43.1	-22.43	LSS
A1190	167.946	40.857	0.076	14.37	636	1.01	17.77	250	CIRS	167.932	40.821	0.7	-5.0	-23.26	LSS
A1201	168.229	13.445	0.167	14.42	683	0.99	19.5	121	HeCS	168.227	13.436	0.63	144.6	-23.87	LSS
A1204	168.332	17.594	0.171	14.05	532	0.74	19.5	55	HeCS	168.335	17.595	0.71	53.6	-22.84	no LSS
A1205	168.468	2.475	0.076	14.31	591	0.96	17.77	145	CIRS	168.462	2.481	0.76	135.7	-22.52	LSS
RXCJ1115.5+5426	168.832	54.434	0.07	14.43	610	1.05	17.77	122	CIRS	168.849	54.444	0.77	-10.4	-23.49	LSS
SHK352	170.418	2.893	0.048	14.44	602	1.05	17.77	75	CIRS	170.382	2.752	0.8	176.6	-22.61	LSS

Table B1: Full list of clusters considered. Columns described in Appendix B text

(i) Name	(ii) RA (deg)	(iii) Dec (deg)	(iv) z	(v) Log(M_{200}) $M_{200}(M_{\odot})$	(vi) σ (km/s)	(vii) R_{200} (Mpc)	(viii) r-mag $_{lim}$ (apparent)	(ix) N_{mem}	(x) Survey	(xi) RA $_{bcg}$ (deg)	(xii) Dec $_{bcg}$ (deg)	(xiii) Ellip $_{bcg}$	(xiv) PA $_{bcg}$ (deg)	(xv) r-mag $_{bcg}$ (absolute)	(xvi) LSSflag
A1235	170.804	19.616	0.103	14.18	584	0.84	19.5	121	HeCS	170.816	19.596	0.58	127.5	-22.49	LSS
A1246	170.991	21.49	0.192	14.71	906	1.22	19.5	161	HeCS	170.995	21.479	0.77	80.2	-22.79	no LSS
A1272	172.468	23.792	0.137	13.93	505	0.69	17.77	37	HeCS-SZ	172.503	23.786	0.82	96.2	-22.51	LSS
A1291B	173.033	56.001	0.058	13.88	508	0.69	17.77	23	CIRS	173.05	56.048	0.98	8.3	-22.1	no LSS
A1291A	173.093	55.98	0.051	13.73	363	0.61	17.77	39	CIRS	173.097	55.967	0.76	82.1	-21.91	LSS
A1307	173.221	14.469	0.081	14.62	756	1.18	17.77	95	HeCS-SZ	173.213	14.461	0.83	2.5	-23.14	LSS
A1302	173.307	66.399	0.115	14.32	650	0.93	19.5	149	HeCS	173.311	66.38	0.73	115.7	-23.73	LSS
A1314	173.618	49.084	0.033	14.24	592	0.9	17.77	112	CIRS	173.705	49.078	0.72	91.4	-22.57	LSS
A1361	175.917	46.374	0.116	14.1	512	0.78	19.5	108	HeCS	175.915	46.356	0.77	144.6	-23.25	LSS
A1367	176.152	19.759	0.023	14.52	716	1.12	17.77	383	HeCS-SZ	176.009	19.95	0.78	1.9	-22.6	LSS
A1366	176.202	67.413	0.116	14.28	616	0.9	19.5	160	HeCS	176.153	67.406	0.7	88.0	-23.46	LSS
A1377	176.846	55.738	0.052	14.12	616	0.83	17.77	103	CIRS	176.839	55.73	0.81	64.3	-22.78	LSS
A1413	178.826	23.408	0.141	14.76	856	1.29	19.5	114	HeCS	178.825	23.405	0.43	174.0	-24.13	no LSS
A1423	179.342	33.632	0.214	14.57	759	1.09	19.5	134	HeCS	179.322	33.611	0.6	61.0	-23.58	no LSS
A1424	179.387	5.088	0.075	14.44	619	1.06	17.77	104	CIRS	179.371	5.089	0.72	71.8	-23.12	LSS
A1436	180.014	56.238	0.065	13.93	501	0.72	17.77	92	CIRS	180.084	56.286	0.62	39.6	-22.27	LSS
A1437	180.104	3.349	0.133	15.03	1233	1.59	19.5	136	HeCS	180.106	3.347	0.6	45.6	-24.01	LSS
A1446	180.5	58.048	0.103	14.15	594	0.82	17.77	44	HeCS-SZ	180.516	58.036	0.89	85.7	-22.91	LSS
MKW4	181.116	1.845	0.02	14.22	577	0.9	17.77	126	CIRS	181.113	1.896	0.7	101.0	-22.82	LSS
RXCJ1210.3+0523	182.579	5.369	0.076	13.86	438	0.68	17.77	67	CIRS	182.57	5.386	0.82	117.6	-23.58	LSS
Zw1215	184.446	3.678	0.077	14.4	735	1.02	17.77	164	CIRS	184.421	3.656	0.84	46.2	-22.91	LSS
NGC4325	185.837	10.582	0.026	13.18	484	0.4	17.77	22	CIRS	185.778	10.621	0.65	3.4	-22.13	LSS
Virgo	186.634	12.723	0.004	14.3	776	0.95	17.77	113	CIRS	187.454	13.429	0.57	93.0	-22.03	LSS
A1552	187.451	11.801	0.086	14.25	711	0.92	17.77	142	CIRS	187.551	11.745	0.93	111.2	-23.0	LSS
A1553	187.696	10.561	0.167	14.66	867	1.19	19.5	131	HeCS	187.704	10.546	0.46	128.3	-23.89	LSS
A1589	190.33	18.571	0.071	14.62	764	1.19	17.77	146	HeCS-SZ	190.323	18.575	0.7	70.7	-23.42	LSS
NGC4636	190.708	2.688	0.003	13.08	232	0.38	17.77	13	CIRS	190.096	3.118	0.86	60.0	-17.81	LSS
A1650	194.646	-1.574	0.084	14.02	524	0.77	17.77	59	CIRS	194.659	-1.575	0.94	106.8	-22.56	LSS
Coma	194.93	27.939	0.023	14.65	827	1.24	17.77	862	HeCS-SZ	195.034	27.977	0.6	80.5	-23.09	LSS
A1663	195.727	-2.501	0.084	14.6	720	1.2	17.77	204	CIRS	195.719	-2.516	0.7	0.7	-23.38	LSS
A1668	195.94	19.271	0.064	14.55	725	1.13	17.77	138	HeCS-SZ	195.944	19.272	0.77	72.0	-23.23	LSS
A1682	196.728	46.556	0.227	14.79	996	1.28	19.5	100	HeCS	196.708	46.559	0.73	153.5	-23.85	no LSS
MS1306	197.33	-1.622	0.083	13.76	409	0.63	17.77	41	CIRS	197.33	-1.623	0.82	9.9	-23.18	LSS
A1691	197.791	39.218	0.072	14.43	733	1.03	17.77	148	HeCS-SZ	197.786	39.227	0.91	142.6	-23.58	LSS
A1689	197.875	-1.335	0.184	14.94	1197	1.46	19.5	164	HeCS	197.873	-1.341	0.82	111.4	-23.25	LSS
A1728	200.572	11.222	0.09	14.47	790	1.08	17.77	85	CIRS	200.594	11.215	0.76	142.6	-22.65	LSS
RXJ1326.2+0013	201.573	0.221	0.083	13.76	481	0.63	17.77	46	CIRS	201.573	0.221	0.76	43.0	-23.67	LSS
MKW11	202.38	11.789	0.023	13.53	361	0.53	17.77	69	CIRS	202.34	11.735	0.73	183.0	-21.87	LSS
A1750	202.708	-1.875	0.086	14.2	643	0.88	17.77	158	CIRS	202.711	-1.862	0.82	60.7	-23.04	LSS
A1758	203.18	50.55	0.276	14.35	674	0.9	19.5	48	HeCS	203.16	50.56	0.76	184.5	-23.42	no LSS
A1763	203.826	40.997	0.231	15.09	1261	1.62	19.5	158	HeCS	203.834	41.001	0.88	92.5	-23.72	no LSS

Table B1: Full list of clusters considered. Columns described in Appendix B text

(i) Name	(ii) RA (deg)	(iii) Dec (deg)	(iv) z	(v) Log(M_{200}) $M_{200}(M_{\odot})$	(vi) σ (km/s)	(vii) R_{200} (Mpc)	(viii) r-mag _{lim} (apparent)	(ix) N_{mem}	(x) Survey	(xi) RA_{bcg} (deg)	(xii) Dec_{bcg} (deg)	(xiii) Ellip _{bcg}	(xiv) PA_{bcg} (deg)	(xv) r-mag _{bcg} (absolute)	(xvi) LSSflag
A1767	204.11	59.162	0.071	14.78	805	1.37	17.77	253	CIRS	204.035	59.206	0.83	159.3	-23.42	LSS
A1775	205.474	26.372	0.075	14.12	556	0.81	17.77	91	HeCS-SZ	205.455	26.373	0.83	158.4	-23.48	LSS
RXJ1342+0213	205.523	2.228	0.077	14.41	746	1.02	17.77	25	HeCS-SZ	205.623	2.201	0.96	144.7	-22.15	LSS
A1773	205.547	2.211	0.078	14.3	615	0.95	17.77	113	CIRS	205.54	2.227	0.6	224.7	-22.73	LSS
A1795	207.221	26.596	0.063	14.52	774	1.11	17.77	180	HeCS-SZ	207.231	26.617	0.86	22.1	-21.36	LSS
A1800	207.34	28.104	0.076	14.68	687	1.24	17.77	167	HeCS-SZ	207.348	28.107	0.61	158.3	-23.8	LSS
RXJ1351.7+4622	208.001	46.237	0.063	13.58	361	0.55	17.77	66	CIRS	207.926	46.185	0.68	184.4	-21.81	LSS
A1809	208.309	5.168	0.079	14.12	551	0.83	17.77	110	CIRS	208.277	5.15	0.79	58.7	-23.55	LSS
A1831	209.823	27.973	0.075	14.63	1178	1.2	17.77	132	HeCS-SZ	209.813	27.976	0.75	158.6	-23.49	LSS
A1835	210.26	2.88	0.251	14.92	1151	1.41	19.5	138	HeCS	210.259	2.878	0.8	152.2	-24.07	no LSS
A1885	213.424	43.66	0.088	14.65	687	1.25	17.77	24	CIRS	213.431	43.645	0.88	105.8	-22.39	LSS
A1902	215.423	37.296	0.162	14.37	784	0.95	19.5	94	HeCS	215.419	37.292	0.77	131.1	-23.8	LSS
A1918	216.342	63.183	0.139	14.29	545	0.9	19.5	41	HeCS	216.344	63.198	0.41	43.8	-23.72	LSS
A1914	216.507	37.827	0.166	14.68	798	1.2	19.5	201	HeCS	216.486	37.816	0.78	64.9	-23.65	LSS
A1925	217.117	56.883	0.105	14.28	606	0.91	17.77	51	HeCS-SZ	217.16	56.861	0.46	131.2	-23.89	LSS
A1930	218.12	31.633	0.131	14.27	577	0.89	19.5	62	HeCS	218.158	31.647	0.75	187.5	-23.65	LSS
MKW8	220.166	3.479	0.027	13.64	325	0.57	17.77	125	CIRS	220.178	3.465	0.73	103.8	-22.53	LSS
A1978	222.775	14.611	0.146	13.94	404	0.69	19.5	61	HeCS	222.789	14.612	0.62	99.2	-24.03	LSS
A1986	223.28	21.895	0.117	13.86	516	0.66	17.77	73	HeCS-SZ	223.258	21.939	0.72	47.5	-22.22	LSS
A2009	225.085	21.362	0.152	14.55	715	1.09	19.5	148	HeCS	225.081	21.369	0.56	171.1	-23.3	LSS
A2018	225.278	47.299	0.087	14.25	585	0.89	17.77	72	HeCS-SZ	225.283	47.277	0.95	157.2	-23.86	LSS
RXJ1504	226.032	-2.805	0.217	14.33	779	0.91	19.5	75	HeCS	226.031	-2.805	0.63	68.3	-23.59	no LSS
NGC5846	227.057	1.635	0.006	13.56	399	0.54	17.77	32	CIRS	226.782	1.544	0.86	116.9	-21.25	LSS
A2034	227.545	33.506	0.113	14.7	942	1.25	19.5	172	HeCS	227.549	33.486	0.57	193.7	-23.62	LSS
A2029	227.729	5.72	0.077	14.71	954	1.27	17.77	379	HeCS-SZ	227.733	5.742	0.64	13.8	-19.42	LSS
A2050	229.068	0.089	0.119	14.64	869	1.18	19.5	108	HeCS	229.075	0.089	0.56	43.4	-23.58	LSS
A2051	229.142	-0.948	0.118	13.63	437	0.55	17.77	58	HeCS-SZ	229.184	-0.969	0.75	133.6	-22.95	LSS
A2055	229.672	6.211	0.102	14.33	676	0.94	19.5	133	HeCS	229.691	6.232	0.95	161.9	-22.81	LSS
A2064	230.256	48.659	0.074	14.22	599	0.89	17.77	81	CIRS	230.218	48.661	0.65	93.3	-23.33	LSS
A2061	230.299	30.683	0.078	14.72	720	1.31	17.77	212	CIRS	230.336	30.671	0.83	55.0	-23.63	LSS
A2065	230.601	27.697	0.073	14.53	1084	1.11	17.77	219	HeCS-SZ	230.622	27.708	0.65	167.3	-22.73	LSS
A2063	230.772	8.603	0.034	14.43	714	1.04	17.77	254	HeCS-SZ	230.772	8.609	0.85	32.0	-22.54	LSS
A2067	230.779	30.869	0.074	13.61	500	0.56	17.77	28	CIRS	230.785	30.878	0.81	183.9	-22.7	no LSS
A2069	231.041	29.921	0.114	14.84	994	1.39	19.5	383	HeCS	231.1	30.006	0.6	150.3	-23.62	LSS
A2107	234.91	21.789	0.041	14.28	590	0.92	17.77	176	HeCS-SZ	234.913	21.783	0.65	115.0	-23.33	LSS
A2111	234.934	34.416	0.229	14.46	741	1.0	19.5	127	HeCS	234.919	34.424	0.69	176.0	-22.93	no LSS
A2110	234.935	30.715	0.097	14.24	581	0.91	17.77	59	CIRS	234.962	30.718	0.63	90.1	-23.22	LSS
RXJ1540+1752	235.038	17.878	0.09	14.04	649	0.76	17.77	43	HeCS-SZ	235.079	17.856	0.71	67.9	-22.56	LSS
A2124	236.226	36.115	0.068	14.78	841	1.38	17.77	185	CIRS	236.246	36.109	0.79	148.2	-23.45	LSS
A2142	239.612	27.178	0.09	14.53	764	1.13	17.77	290	CIRS	239.583	27.233	0.71	133.3	-23.69	LSS
A2149	240.347	54.02	0.065	13.04	276	0.36	17.77	48	CIRS	240.367	53.947	0.82	119.8	-22.97	LSS

Table B1: Full list of clusters considered. Columns described in Appendix B text

(i) Name	(ii) RA (deg)	(iii) Dec (deg)	(iv) z	(v) Log(M_{200}) $M_{200}(M_{\odot})$	(vi) σ (km/s)	(vii) R_{200} (Mpc)	(viii) r-mag $_{lim}$ (apparent)	(ix) N_{mem}	(x) Survey	(xi) RA_{bcg} (deg)	(xii) Dec_{bcg} (deg)	(xiii) Ellip $_{bcg}$	(xiv) PA_{bcg} (deg)	(xv) r-mag $_{bcg}$ (absolute)	(xvi) LSSflag
A2147	240.578	16.02	0.036	14.47	715	1.07	17.77	535	HeCS-SZ	240.571	15.975	0.65	190.9	-22.74	LSS
A2169	243.466	49.133	0.059	13.97	478	0.74	17.77	74	CIRS	243.492	49.19	0.69	86.3	-22.14	LSS
NGC6107	244.433	35.05	0.031	14.02	464	0.77	17.77	80	CIRS	244.419	35.004	0.89	64.5	-22.49	LSS
A2175	245.132	29.895	0.096	14.33	644	0.95	19.5	182	HeCS-SZ	245.13	29.891	0.75	147.1	-22.65	LSS
A2187	246.059	41.238	0.183	14.1	631	0.77	19.5	76	HeCS	246.058	41.244	0.63	56.6	-23.64	no LSS
A2199	247.169	39.549	0.031	14.38	676	1.01	17.77	366	CIRS	247.159	39.551	0.78	213.7	-22.83	LSS
A2197	247.477	40.663	0.03	13.86	535	0.68	17.77	216	CIRS	247.437	40.812	0.66	139.2	-23.47	LSS
A2219	250.089	46.706	0.226	14.95	1151	1.46	19.5	262	HeCS	250.083	46.711	0.66	113.9	-23.17	no LSS
A2245	255.617	33.497	0.087	14.73	952	1.32	17.77	148	CIRS	255.638	33.517	0.88	230.5	-23.52	LSS
A2244	255.624	34.03	0.1	14.63	981	1.23	17.77	92	CIRS	255.677	34.06	0.72	171.3	-23.95	LSS
A2256	255.953	78.644	0.058	14.9	1101	1.48	19.5	261	HeCS-SZ	256.113	78.64	0.87	136.5	-23.22	no LSS
A2249	257.453	34.441	0.085	14.37	778	0.98	17.77	98	HeCS-SZ	257.41	34.431	0.7	214.9	-22.57	LSS
A2255	258.139	64.042	0.08	14.88	961	1.48	17.77	279	CIRS	258.145	64.071	0.77	84.2	-23.52	no LSS
NGC6338	258.842	57.425	0.029	14.18	492	0.87	17.77	152	CIRS	258.846	57.411	0.77	198.5	-22.72	no LSS
Zw8193	259.329	42.444	0.182	14.68	899	1.2	19.5	124	HeCS-SZ	259.33	42.45	0.55	143.0	-22.87	LSS
Zw8197	259.548	56.671	0.113	14.26	597	0.89	19.5	75	HeCS	259.55	56.666	0.65	96.3	-22.79	no LSS
A2259	260.037	27.67	0.161	14.58	855	1.12	19.5	158	HeCS	260.04	27.669	0.5	107.7	-23.77	LSS
RXJ1720	260.037	26.635	0.16	14.65	860	1.18	19.5	167	HeCS	260.042	26.626	0.8	197.9	-23.46	LSS
A2261	260.613	32.134	0.224	14.42	780	0.97	19.5	217	HeCS	260.613	32.133	0.86	171.1	-24.52	no LSS
Zw8284	266.82	45.216	0.158	14.24	564	0.86	19.5	101	HeCS-SZ	266.808	45.195	0.6	210.7	-23.32	no LSS
IC1365	318.474	2.556	0.05	14.26	575	0.91	17.77	85	HeCS-SZ	318.528	2.462	0.89	33.2	-22.28	no LSS
RXJ2129	322.419	0.097	0.234	14.75	858	1.24	19.5	111	HeCS	322.416	0.089	0.51	68.1	-23.44	no LSS
A2355	323.818	1.4	0.231	14.71	911	1.21	19.5	15	HeCS-red	323.828	1.424	0.88	104.4	-23.03	no LSS
A2390	328.398	17.697	0.228	15.08	1278	1.61	19.5	148	HeCS-red	328.403	17.695	0.69	132.7	-23.14	no LSS
A2396	328.92	12.534	0.192	14.58	935	1.11	19.5	131	HeCS	328.925	12.525	0.84	14.9	-23.76	no LSS
A2399	329.362	-7.819	0.058	14.0	532	0.76	17.77	123	CIRS	329.257	-7.84	0.7	105.1	-22.95	no LSS
A2409	330.22	20.971	0.145	14.68	839	1.22	19.5	176	HeCS-SZ	330.219	20.969	0.8	-4.8	-23.12	no LSS
RMJ220107d7p111805d2	330.281	11.298	0.238	14.15	560	0.78	19.5	56	HeCS-red	330.282	11.301	0.72	136.5	-23.19	no LSS
A2415	331.419	-5.593	0.058	14.43	720	1.04	17.77	84	OmegaWINGS	331.359	-5.742	0.73	26.5	-22.76	no LSS
RXCJ2214.8+1350	333.662	13.83	0.026	13.46	360	0.5	17.77	59	CIRS	333.687	13.847	0.82	44.1	-22.42	no LSS
A2428	334.085	-9.332	0.084	14.16	487	0.85	17.77	60	CIRS	334.065	-9.333	0.72	50.0	-23.57	no LSS
A2440	335.971	-1.638	0.091	14.55	812	1.12	19.5	132	HeCS-SZ	335.987	-1.583	0.89	64.8	-23.29	no LSS
A2443	336.511	17.378	0.11	14.28	619	0.9	19.5	79	HeCS-SZ	336.533	17.357	0.82	46.8	-23.47	no LSS
A2454	338.551	5.813	0.165	14.68	934	1.2	19.5	114	HeCS-SZ	338.598	5.838	0.79	60.8	-23.39	no LSS
A2457	338.938	1.476	0.059	14.29	641	0.92	17.77	164	OmegaWINGS	338.92	1.485	0.7	86.9	-23.39	no LSS
A2495	342.587	10.902	0.079	14.14	634	0.82	19.5	141	HeCS-SZ	342.582	10.903	0.63	50.3	-22.99	no LSS
RMJ225946d5p310223d9	344.956	31.037	0.194	14.41	661	0.98	19.5	97	HeCS-red	344.944	31.04	0.97	94.3	-22.88	no LSS
PegasusII	347.61	7.577	0.041	14.5	740	1.1	17.77	80	HeCS-SZ	347.593	7.581	0.69	16.2	-22.74	no LSS
A2593	351.102	14.672	0.042	14.35	570	0.99	17.77	226	CIRS	351.084	14.647	0.64	75.7	-22.82	no LSS
RMJ232626d2p292152d7	351.609	29.351	0.227	14.56	938	1.08	19.5	34	HeCS-red	351.609	29.365	0.67	156.0	-23.73	no LSS
A2623	353.742	5.646	0.194	14.59	765	1.12	19.5	95	HeCS-SZ	353.712	5.618	0.87	174.2	-22.94	no LSS

Table B1: Full list of clusters considered. Columns described in Appendix B text

(i) Name	(ii) RA (deg)	(iii) Dec (deg)	(iv) z	(v) Log(M_{200}) $M_{200}(M_{\odot})$	(vi) σ (km/s)	(vii) R_{200} (Mpc)	(viii) r-mag/ i_{m} (apparent)	(ix) N_{mem}	(x) Survey	(xi) RA_{bcg} (deg)	(xii) Dec_{bcg} (deg)	(xiii) Ellip $_{\text{bcg}}$	(xiv) PA_{bcg} (deg)	(xv) r-mag $_{\text{bcg}}$ (absolute)	(xvi) LSSflag
A2631	354.421	0.276	0.277	14.58	851	1.07	19.5	64	HeCS	354.416	0.271	0.73	87.0	-23.56	no LSS
A2645	355.32	-9.028	0.251	13.87	549	0.63	19.5	35	HeCS	355.321	-9.02	0.83	22.2	-23.04	no LSS
RXJ2344-0422	356.067	-4.368	0.079	14.27	543	0.91	19.5	119	HeCS-SZ	356.076	-4.38	0.76	143.9	-23.41	no LSS
MS2348+2929	357.64	29.498	0.154	13.94	525	0.69	19.5	74	HeCS-SZ	357.651	29.492	0.88	114.6	-22.03	no LSS
A2665	357.711	6.161	0.056	14.05	554	0.77	19.5	121	HeCS-SZ	357.711	6.15	0.84	115.4	-23.31	no LSS
A2670	358.578	-10.417	0.076	14.27	687	0.93	17.77	159	CIRS	358.557	-10.419	0.92	95.7	-23.42	no LSS

Table C1. Number of segments of the LSS in each subsample of the ‘Cluster Members + LSS’ sample from Figure 2

Radius	Subsample	BCG shape	Nconnect	R _{200,connect}	Near Pair	LSS weight
		[0 – 3] R ₂₀₀	958	235	2033	1112
[3 – 6] R ₂₀₀	808	303	1702	1044	1480	
[6 – 10] R ₂₀₀	1591	515	3018	1650	2334	
[0 – 10] R ₂₀₀	3357	1053	6753	3806	5542	

Table C2. Number of galaxies in each subsample of the ‘Cluster Members only’ sample from Figure 3

Radius	Subsample	BCG shape	Cluster Mass	Luminosity	Nearby Universe	Near Pair	Completeness	N _{mem,min}
		[0 – 1] R ₂₀₀	6728	6252	6262	7679	7175	6800
[1 – 2] R ₂₀₀	3373	3369	2909	3871	4229	3699	5739	
[2 – 3] R ₂₀₀	1988	1905	1449	2197	2554	2371	3526	
[0 – 3] R ₂₀₀	11639	11526	10620	13747	13958	12872	18948	

Table C3. Number of clusters in each subsample of the ‘Cluster Members + LSS’ sample in Figure 2

Fiducial	BCG shape		Nconnect			R _{200,connect}	Near Pair		LSS Weighting
	Round	Ellip	=2	=3	≥4	1	>10 R ₂₀₀	No Limit	No Weight
91	43	48	24	28	39	64	55	124	86

Table C4. Number of clusters in each subsample of the ‘Cluster Members only’ sample in Figure 3

All	BCG shape		Cluster Mass		Luminosity		Nearby Universe	Near Pair		Completeness	N _{mem,min}
	Round	Ellip	High	Low	Bright	Faint	z<0.1	>10 R ₂₀₀	>5 R ₂₀₀	High	N _{sat>100}
211	105	106	74	137	211	211	108	131	172	104	112

APPENDIX C: TABLES WITH NUMBER OF OBJECTS IN EACH SUBSAMPLE

This paper has been typeset from a $\text{\TeX}/\text{\LaTeX}$ file prepared by the author.